

Nonlinear Myofilament Regulatory Processes Affect Frequency-Dependent Muscle Fiber Stiffness

Kenneth B. Campbell,^{*†} Maria V. Razumova,[‡] Robert D. Kirkpatrick,^{*} and Bryan K. Slinker^{*}

^{*}Department of Veterinary and Comparative Anatomy, Pharmacology and Physiology, [†]Department of Biological Systems Engineering, Washington State University, Pullman, Washington 99163, and [‡]Department of Physiology, University of Wisconsin–Madison, Madison, Wisconsin 53706 USA

ABSTRACT To investigate the role of nonlinear myofilament regulatory processes in sarcomeric mechanodynamics, a model of myofilament kinetic processes, including thin filament on–off kinetics and crossbridge cycling kinetics with interactions within and between kinetic processes, was built to predict sarcomeric stiffness dynamics. Linear decomposition of this highly nonlinear model resulted in the identification of distinct contributions by kinetics of recruitment and by kinetics of distortion to the complex stiffness of the sarcomere. Further, it was established that nonlinear kinetic processes, such as those associated with cooperative neighbor interactions or length-dependent crossbridge attachment, contributed unique features to the stiffness spectrum through their effect on recruitment. Myofilament model-derived sarcomeric stiffness reproduces experimentally measured sarcomeric stiffness with remarkable fidelity. Consequently, characteristic features of the experimentally determined stiffness spectrum become interpretable in terms of the underlying contractile mechanisms that are responsible for specific dynamic behaviors.

INTRODUCTION

The frequency-dependent, complex stiffness of muscle fibers has value for several reasons: 1) for characterizing the contractile status of one fiber to compare it with other fibers; 2) for predicting physiologic function of fibers; and 3) for inferring underlying contractile mechanisms. These values were recognized early by those who worked on insect flight muscle (Machin and Pringle, 1960; Pringle, 1978; Abbot and Steiger, 1977; Thorson and White, 1983) and by Kawai and colleagues who applied muscle stiffness techniques to vertebrate striated muscle. These latter workers developed a theoretical basis for interpreting experimentally obtained complex muscle stiffness in terms of crossbridge (XB) kinetic processes (Kawai and Brandt, 1980; Kawai and Halvorson, 1989; Kawai et al., 1993; Saeki et al., 1991; Zhao and Kawai, 1993, 1996) and these ideas have been adopted and extended by several others (Blanchard et al., 1999; Dickinson et al., 1997; Maughan et al., 1998; Murase et al., 1986; Smith, 1990; Thomas and Thornhill, 1996; Wannenburg et al., 2000).

Recent work from our laboratory (Campbell, 1997; Razumova et al., 1999, 2000) has implicated myofilament regulatory proteins as significant determinants of the dynamic behavior of constantly activated myofilament systems. These regulatory actions are expressed in fiber dynamics through cooperative and other nonlinear mechanisms and contribute to fiber dynamics in such a way that they confound the observation of XB cycle kinetic steps.

Therefore, the purpose of the present work was to incorporate nonlinear regulatory mechanisms into a myofilament model of the sarcomere for the purpose of examining how these nonlinear regulatory mechanisms impact complex stiffness of the sarcomere and, thus, muscle fibers. We give special emphasis to cardiac muscle because of its peculiar length-dependent dynamic behavior.

INTERPRETING SARCOMERIC COMPLEX STIFFNESS IN TERMS OF MYOFILAMENT KINETICS

Myofilament kinetic model

A mathematical model of the sarcomere was built based on kinetics within the myofilament system. In the simplest conceptualization of myofilament kinetics (Fig. 1), there are three kinetic processes responsible for muscle dynamics: 1) the kinetics of activator Ca^{2+} availability to myofilaments; 2) the kinetics of thin-filament regulatory process by which the troponin–tropomyosin regulatory units (RU) change position on the thin filament in switching from a position that blocks to one that permits myosin attachment to actin on the thin filament; and 3) the kinetics of the XB cycle, during which there is chemomechanical energy transduction accompanying actin-activated, myosin-catalyzed ATP hydrolysis.

We assumed that Ca^{2+} -binding to the tropomyosin–troponin regulatory protein complex was both relatively fast and independent of other kinetic processes. Accordingly, Ca^{2+} -binding kinetics may be reduced to Ca^{2+} -binding isotherms to the troponin C subunit (TnC) as given in the Appendix, Eqs. A12, and A13.

Thin-filament regulatory kinetics involve switching the tropomyosin–troponin RU between an off state that does not permit XB attachment and an on state that permits attach-

Received for publication 3 April 2001 and in final form 18 July 2001.

Address reprint requests to Kenneth B. Campbell, Department of VCAPP, Washington State University, Pullman, WA 99163. Tel.: 509-335-8011; Fax: 509-335-4650; E-mail: cvsclkbc@vetmed.wsu.edu.

© 2001 by the Biophysical Society

0006-3495/01/10/2278/19 \$2.00

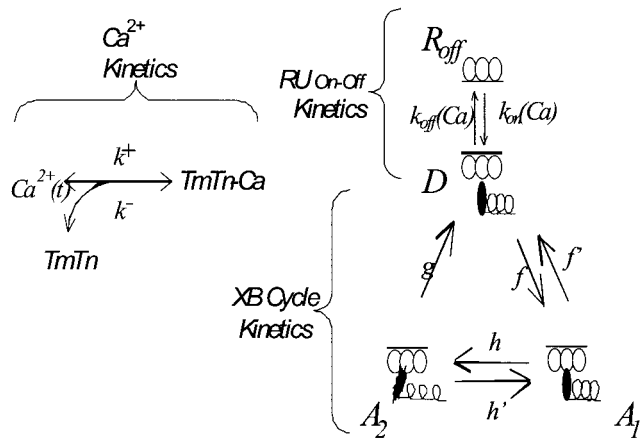


FIGURE 1 Three kinetic processes in myofibril interaction showing: 1) Ca^{2+} binding to the tropomyosin-troponin complex that acts as the thin-filament RU; 2) switching between off and on states of the RU; and 3) myosin XB cycling between attached and detached states. The forward, k^+ , and backward, k^- , Ca^{2+} binding constants are taken to be large with respect to other kinetic constants and independent of other steps in the contraction process, such that Ca^{2+} binding is always in equilibrium. The three connected circles represent the thin filament. The bar along the thin filament represents the RU. In the up position, the RU is off and XBs cannot attach. In the down position, the RU is on and XBs can attach. The rate coefficients regulating the transition between on and off states, $k_{\text{on}}(\text{Ca})$ and $k_{\text{off}}(\text{Ca})$, are functions of Ca^{2+} bound to RU as given in the text. The darkened ellipse with the coiled tail represents the XB, which may be in one of three states: detached, D, attached pre-power-stroke, A_1 , or attached and post-power-stroke, A_2 .

ment. RU on-off switching depends on whether Ca^{2+} is bound to TnC. Thus, we identify four rate coefficients for RU on-off state transitions: k_{on}^0 ; k_{off}^0 ; $k_{\text{on}}^{\text{Ca}}$; $k_{\text{off}}^{\text{Ca}}$, where the superscript indicates whether Ca^{2+} is bound to the TnC part of the RU. For any Ca^{2+} level, the net values of the on-off coefficients are given by

$$k_{\text{on}} = k_{\text{on}}^0 + (k_{\text{on}}^{\text{Ca}} - k_{\text{on}}^0)[\text{Ca}^{2+} \text{ binding isotherm}]$$

and

$$k_{\text{off}} = k_{\text{off}}^0 + (k_{\text{off}}^{\text{Ca}} - k_{\text{off}}^0)[\text{Ca}^{2+} \text{ binding isotherm}].$$

XB cycling kinetics requires representing transitions among at least three states: detached, D; attached pre-power stroke, A_1 ; and attached post-power stroke, A_2 . The transition between states D and A_1 is the attachment step; the transition between states A_1 and A_2 is the power stroke; and the transition between states A_2 and D is the detachment step. Because chemomechanical energy transduction takes place in the power stroke, the pre-power stroke attached state, A_1 , does not bear force except in nonisometric conditions when the sarcomere undergoes length change and there is shearing between thick and thin filaments. In contrast, the post-power stroke attached state, A_2 , is force bearing in both isometric and nonisometric conditions. We treat the attachment step and the power stroke as reversible,

but we treat the detachment step as irreversible. Steps in the XB cycle are regulated by the rate coefficients f , f' , h , h' , and g , which determine the rate of change between states according to Fig. 1.

Length-dependent processes within the myofibril system occur as a result of sliding filament and nonlinear kinetic mechanisms

Fundamental to any myocardial myofibril model are mechanisms that account for well-known length-dependent processes in cardiac muscle such as length-tension behavior and length-dependent Ca^{2+} sensitivity. The three kinetic processes (Ca^{2+} binding, RU on-off transitions, and XB cycling) all take place on a sliding myofibril system where overlap between thick and thin filaments changes when the sarcomere changes length. Thus, through filament sliding alone, the three kinetic processes become coupled to sarcomere length, L_S . Additionally, nonlinear mechanisms also couple these kinetic processes to L_S through either structurally-coupled or cooperatively-coupled pathways.

There are four categories of nonlinear mechanisms that impact myofibril kinetics: saturation, cooperativity, length-dependent kinetic steps, and strain-dependent kinetic steps. Of these, strain-dependent kinetic steps, following the work of Huxley (1957), have been central in most attempts at modeling contractile system behavior. However, by restricting our concern to small amplitude perturbations around an isometric state, strain-dependence in the kinetic steps may be excluded as if variation in XB strain energy is occurring around the bottom of a strain-energy well (Thorson and White, 1983). Once strain-dependent phenomena are excluded, it is possible to focus on the other nonlinearities. Such a focus distinguishes our analysis from several others, where attempts to reproduce aspects of frequency-dependent muscle stiffness relied heavily on strain-dependent XB cycling kinetic steps (Murase et al., 1986; Smith, 1990; Thomas and Thornhill, 1996). Of the remaining three nonlinear categories, we are interested here in nonlinear dynamic effects arising from responses to changes in L_S . These consist of two types of effects; those that are closely coupled to L_S and work through structural mechanisms (structurally coupled) and those that are loosely coupled to L_S and work through cooperative mechanisms (cooperatively coupled).

Structurally-coupled effects give rise to a force response with only one or two intervening events following a muscle length perturbation. The sliding filament mechanism is an obvious example in that changes in L_S change filament overlap and this changes the number of available sites for myosin XB attachment to actin. Changes in XB-attachment site number leads to changes in the number of attached XB with concomitant changes in the ensuing force. In the model, sliding filament mechanisms are the consequence of fixed myofibril lengths and their overlapping arrange-

ment (Eqs. A7–A11) and are not graded with an adjustable parameter. Another structurally-coupled effect arises when an increase in L_S causes a decrease in myofilament lattice spacing. Decreased interfilament spacing reduces the distance that the myosin head must travel to attach to the actin binding site and, thus, reduces the activation energy barrier for XB attachment (Godt and Maughan, 1981; McDonald and Moss, 1995; Fuchs and Smith, 2001). The result is that the probability for myosin attachment to actin increases. For this reason, we changed the f - f' coefficient pair with changes in L_S because this is the attachment step in our XB scheme. We had no rationale for changing h , h' , and g with sarcomere length and, therefore, we did not allow these coefficients to be length sensitive. To account for expression of length-dependent XB attachment, a formulation based on activation energy variations, as these affect the f - f' coefficient pair, was derived, Eqs. A16 and A17. The single arbitrary parameter, β , was used in Eqs. A16 and A17 to grade the strength of these length-dependent effects.

Cooperatively-coupled effects give rise to a secondary force following a primary length-induced force event. For instance, because of the elastic properties of the strongly-bound XB (A_2 state, Fig. 1), this XB is strained and undergoes a change in force immediately upon a change in L_S . This change in force may affect the strength of influence of this strongly bound XB on actions at a neighboring site. If this influence is to favor the turning on of a neighboring RU, then we say there is XB–RU neighbor interaction. We vary XB–RU neighbor interactions through the single parameter, w , which impacts the k_{on} - k_{off} coefficient pair according to Eqs. A18 and A19. If the influence of the force exerted by the strongly-bound XB is to influence XB attachment at a neighboring site then we say there is XB–XB interaction. We vary XB–XB neighbor interactions through the single parameter, v , which impacts the f - f' coefficient pair according to Eqs. A20 and A21. Thus, through these cooperative mechanisms, a change in L_S has a primary and immediate force effect on existing XB that then has a secondary force effect through neighbor interactions. In addition to the two preceding cooperative mechanisms, we also varied cooperative interactions between neighboring regulatory units (RU–RU interaction) through the single parameter, u , which impacts the k_{on} - k_{off} coefficient pair according to Eqs. A18 and A19. Equations for these nonlinear cooperative effects have been developed previously (Razumova et al., 2000).

Equations for both structurally coupled and cooperatively coupled L_S responsiveness, together with the differential equations for kinetics of change of state, constitute the essential features of the mathematical model of the sarcomere, Eqs. A1–A21.

Recruitment-distortion concept allows sarcomeric dynamics to be expressed in terms of variables derived from XB population kinetics

In addition to kinetic concepts, a recruitment-distortion concept plays an essential role in the calculation of overall sarcomeric stiffness. This idea evolved from notions first expressed by Huxley (1957), extended and applied by Thorson and White (1983), further applied by Berman et al. (1988), and finally articulated in the version used in this manuscript by Razumova et al. (1999). In the recruitment-distortion concept, the net XB force, $F(t)$, is due to the collective instantaneous stiffness of a population of parallel, attached XB multiplied by their average elastic deformation. In this, we assume that each XB is an elastic spring. If XB in A_1 and A_2 attached states are all in parallel, then

$$F(t) = \eta A_1(t)x_1(t) + \eta A_2(t)x_2(t), \quad (1)$$

where η is the elastic stiffness coefficient of a single XB ($= 4-7 \times 10^{-4}$ N/m); $A_1(t)$ and $A_2(t)$ are the time-dependent system variables representing changing numbers of XB in the A_1 and A_2 states, respectively; and $x_1(t)$ and $x_2(t)$ are the time-dependent system variables representing average elastic deformations (or distortions) of XB in the A_1 and A_2 states, respectively. Note that η is a constant, but all other terms on the right hand side of Eq. 1 are dynamic system variables with time behaviors that are dictated by differential equations (Eqs. A1–A5). Because, for a single half sarcomere, all XB in each state are in parallel, the collective stiffness coefficient of the XB populations in each of the two states may be given as

$$\varepsilon_1(t) = \eta A_1(t) \quad \text{and} \quad \varepsilon_2(t) = \eta A_2(t). \quad (2)$$

Thus,

$$F(t) = \varepsilon_1(t)x_1(t) + \varepsilon_2(t)x_2(t), \quad (3)$$

where the XB population stiffness coefficients, $\varepsilon_1(t)$ and $\varepsilon_2(t)$, are time-dependent variables that change according to $A_1(t)$ and $A_2(t)$, respectively. Because our use of the word “stiffness” takes on multiple nuances as we proceed with an analysis in the frequency domain, we will call $\varepsilon_1(t)$ and $\varepsilon_2(t)$ recruitment variables for the reason that these variables (according to Eq. 2) are proportional to the number of XB that have been recruited into A_1 and A_2 states, respectively. Physically, $\varepsilon_1(t)$ and $\varepsilon_2(t)$ represent instantaneous or infinite-frequency stiffness, and this is a special case of a general complex stiffness as developed below.

Sarcomeric stiffness dynamics are the sum of dynamics due to XB distortion and dynamics due to XB recruitment

The product of two time-varying variables in each term of the recruitment-distortion equation ($\varepsilon_1(t)x_1(t)$ and $\varepsilon_2(t)x_2(t)$ in Eq. 3) complicates stiffness evaluation. In part, these complications arise because this is a nonlinear combination

of variables, all of which depend on L_S . Thus, the experimental determination of stiffness as the ratio, $\Delta F/\Delta L_S$, is meaningful only for incremental changes in force and length around some reference point. We examine these incremental changes with linearization techniques. Linearization of Eq. 3 results in

$$dF(t) = \varepsilon_{10}dx_1(t) + \varepsilon_{20}dx_2(t) + x_{20}d\varepsilon_2(t), \quad (4)$$

where ε_{10} , ε_{20} , and x_{20} are the reference baseline values around which incremental variations in the $\varepsilon_1(t)$, $\varepsilon_2(t)$, and $x_2(t)$ variables occur. The term $x_{10}d\varepsilon_1(t)$ drops out of Eq. 4 because all reference states around which incremental variations are imposed are in the isometric condition and x_{10} , the average distortion of the pre-power stroke A_1 state in the isometric condition, is identically zero. To determine stiffness, the $dF(t)$ dependence on change in sarcomere length, $dL_S(t)$, is required. For this, the linear situation created by restricting our analysis to incremental behaviors allows the following expressions

$$dx_1(t) = H_{x_1}\{dL_S(t)\}, \quad (5)$$

$$dx_2(t) = H_{x_2}\{dL_S(t)\}, \quad (6)$$

$$d\varepsilon_2(t) = H_{\varepsilon_2}\{dL_S(t)\}, \quad (7)$$

where the $H_y\{\}$ are the linear, dynamic transfer operators that convert a $dL_S(t)$ input into $dx_1(t)$, $dx_2(t)$, and $d\varepsilon_2(t)$ responses, respectively. Substituting Eqs. 5–7 into Eq. 4 and Fourier transforming the result gives

$$dF(j\omega) = \varepsilon_{10}H_{x_1}(j\omega)dL_S(j\omega) + \varepsilon_{20}H_{x_2}(j\omega)dL_S(j\omega) + x_{20}H_{\varepsilon_2}(j\omega)dL_S(j\omega), \quad (8)$$

where the $H_y(j\omega)$ are now frequency-dependent transfer functions relating each of the respective variables to sinusoidal $dL_S(j\omega)$. Terms with physical units of stiffness are readily formed by dividing both sides of Eq. 8 by $dL_S(j\omega)$, yielding

$$\underbrace{\frac{dF}{dL_S}(j\omega)}_{\text{sarcomeric stiffness}} = \underbrace{\frac{\varepsilon_{10}H_{x_1}(j\omega)}{x_1 \text{ component}} + \frac{\varepsilon_{20}H_{x_2}(j\omega)}{x_2 \text{ component}}}_{\text{distortion stiffness}} + \underbrace{\frac{x_{20}H_{\varepsilon_2}(j\omega)}{\varepsilon_2 \text{ component}}}_{\text{recruitment stiffness}} \quad (9)$$

The left-hand side of Eq. 9 is the overall frequency-dependent, complex stiffness of the sarcomere. It is composed of the three terms on the right-hand side, each of which arises from different kinetic features of the myofibril system. We designate the first term the x_1 component because its dynamic attributes derive from myofibril

kinetic features responsible for changes in the x_1 distortional variable in response to changes in L_S . We designate the second term the x_2 component because its dynamic attributes derive from myofibril kinetic features responsible for changes in the x_2 distortional variable in response to changes in L_S . Together, the x_1 and x_2 components combine to form a distortional stiffness component of the sarcomeric complex stiffness. We designate the third term the ε_2 component because its dynamic attributes derive from myofibril kinetic features responsible for changes in the ε_2 recruitment variable in response to changes in L_S . Because of the physical sense of the ε_2 component, it may be thought of as a recruitment stiffness. We will see that the ε_2 component possesses dynamic behaviors that are important to the elucidation of length-sensitive mechanisms within the sarcomere.

Model interpretation of frequency domain stiffness components

To relate the three stiffness components to myofibril kinetics, the model's nonlinear, state-variable, differential equations (Eqs. A1–A5) were first linearized by taking a first-order Taylor expansion about some reference state. This linearization procedure is detailed by Eqs. A30–A91 in the Appendix and is summarized here. Let the i indexed upper case Y_i , represent state variables (D , A_1 , A_2 , x_1 , x_2) and the k indexed upper-case, U_m , represent input variables (L_S , Ca). The indexed lower-case y_i and u_i represent respective incremental deviations of state variables and input variables from their reference values. Then, the general form for linearized differential equations is given as

$$\dot{y}_i = \sum_j \partial_i^{Y_j} y_j + \sum_m \partial_i^{U_m} u_m, \quad (10)$$

where the $\partial_i^{Y_j}$ are the values of the partial derivatives of the \dot{Y}_i with respect to the Y_j ($j = 1, 2, 3, 4, 5$) evaluated at the reference state and the $\partial_i^{U_m}$ are the values of the partial derivatives of the \dot{Y}_i with respect to the U_m ($m = 1, 2$) also evaluated at the reference state.

Once the $\partial_i^{Y_j}$ and $\partial_i^{U_m}$ were known, the linear differential equations for incremental variation were formed, they were frequency transformed and substitutions were made to eliminate unwanted state variables. After rearrangement, the transfer functions in Eq. 9 for the x_1 and x_2 components were found in terms of the kinetic rate coefficients of the myofibril system (Eqs. A45–A47) as

$$H_{x_1}(j\omega) = \frac{1}{2} \frac{j\omega[j\omega + (h + g + h')]}{[j\omega]^2 + [h + f' + g + h']j\omega + f'[g + h']}, \quad (11)$$

$$H_{x_2}(j\omega) = \frac{1}{2} \frac{j\omega[j\omega + (h + f' + g + h')]}{[j\omega]^2 + [h + f' + g + h']j\omega + f'[g + h']}. \quad (12)$$

TABLE 1 Model Parameters

Kinetic Parameters	f_0 (s ⁻¹)	f'_0 (s ⁻¹)	h_{iso} (s ⁻¹)	h'_{iso} (s ⁻¹)	g_0 (s ⁻¹)	k_{on}^{Ca} (s ⁻¹)	k_{off}^{Ca} (s ⁻¹)	k_{on}^0 (s ⁻¹)	k_{off}^0 (s ⁻¹)
Generic baseline	50	500	8	6	4	150	50	0	150
Rat trabecular muscle	4.35	791	2.23	2.30	20.0	26.6	38.0	0.0	30,155
Mouse papillary strip	10.7	1023	8.85	1.62	47.7	49.4	39.5	0.0	12,800

Nonlinear Parameters	Length-dependent parameter			Cooperativity parameters		
	β	u	v	w		
Generic baseline (null values)	0	1	1	1		
Rat trabecular muscle	4.49	1.00	4.25	5.33		
Mouse papillary strip	3.01	1.07	4.78	4.68		

Structural Parameters	L_A (μ)	B (μ)	L_M (μ)	R_T	L_R (μ)	x_0 (μ)
Generic baseline	1.2	0.2	1.6	1.62×10^5	1.8	0.01
Rat trabecular muscle	1.2	0.2	1.6	1.62×10^5	1.62	0.11
Mouse papillary strip	1.2	0.2	1.6	1.62×10^5	1.77	0.10

These transfer functions are multiplied by the steady-state values of the recruitment variables (ε_{10} , ε_{20}) to form distortional stiffness according to Eq. 9.

Further substitution and rearrangement of the frequency-transformed linear equations resulted in the following transfer function expression for the ε_2 component, also in terms of kinetic features of the myofilament system,

$$H_{\varepsilon_2}(j\omega) = \frac{[n_5 j\omega + n_4][H_{x_1}(j\omega)] + [n_3 j\omega + n_2][H_{x_2}(j\omega)] + n_1 j\omega + n_0}{[j\omega]^3 + k_2 [j\omega]^2 + k_1 j\omega + k_0} \quad (13)$$

In Eq. 13, the numerator and denominator coefficients, n_i and k_i , are combinations of the $\partial_i^{Y_j}$ and $\partial_i^{U_m}$ (in turn, these partial-derivative terms from the linearization process are combinations of rate coefficients, reference states, and coefficients that grade the strength of the various nonlinearities, according to Eqs. A48–A91). This transfer function is multiplied by x_0 to form the ε_2 component, or recruitment stiffness, as identified in Eq. 9.

The numerator terms in Eq. 13 lead to a natural decomposition of recruitment stiffness into band-pass and low-pass components according to

$$\begin{aligned} & \underbrace{x_0 H_{\varepsilon_2}(j\omega)}_{\text{recruitment stiffness}} \\ &= x_0 \underbrace{\frac{[n_5 j\omega + n_4][H_{x_1}(j\omega)] + [n_3 j\omega + n_2][H_{x_2}(j\omega)]}{[j\omega]^3 + k_2 [j\omega]^2 + k_1 j\omega + k_0}}_{\text{band-pass recruitment stiffness}} \\ & \quad + \underbrace{\frac{n_1 j\omega + n_0}{[j\omega]^3 + k_2 [j\omega]^2 + k_1 j\omega + k_0}}_{\text{low-pass recruitment stiffness}} \quad (14) \end{aligned}$$

The band-pass and low-pass recruitment stiffness components are associated, respectively, with the cooperatively coupled and structurally coupled responses to L_S described

previously. As demonstrated below, the numerator coefficients of the band-pass recruitment component, n_{2-5} , have value only if some forms of cooperativity are operative. In contrast, the numerator coefficients of the low-pass recruitment component, n_{1-0} , have value only if structural mechanisms such as sliding filament or lattice spacing-related XB attachment are operative.

Structurally-coupled and cooperatively-coupled responses to sarcomeric length greatly modify sarcomeric stiffness and step response characteristics

Without length-responsiveness the sarcomere is a dynamic system that exhibits strictly hi-pass filtering characteristics and no positive work features

A generic myofilament baseline condition was defined by: 1) $L_S = 2.3 \mu\text{m}$ (because this L_S is on the plateau of the filament overlap versus L_S relation, there is no change in filament overlap with incremental change in L_S); 2) Ca^{2+} binding isotherm = 1, i.e., full Ca^{2+} saturation; and 3) all model parameters equal to the generic-muscle baseline values given in Table 1. The baseline parameter values in Table 1 were chosen as a compromise because there is no one set of parameters for a general model of striated muscle because of the great diversity among muscles adapted for specific functions in different species, among muscles adapted for different functions within a single organism, and within single muscles undergoing temporal adaptations because of disease, changing use patterns, and mechanical environments. The parameter set given in Table 1 is only representative of a baseline, and one can expect 2–10-fold differences from these values for any given muscle. Importantly, the baseline condition lacked cooperativity, length-dependent XB attachment, and sliding filament recruitment ($\beta = 1$, $u = v = w = 0$).

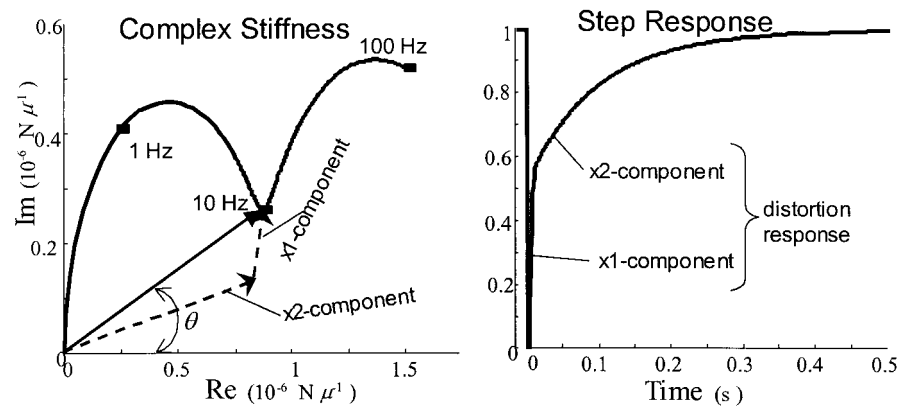


FIGURE 2 *Left panel*, Polar plot of overall complex stiffness for baseline model parameters showing vector composition in terms of x_1 and x_2 components (dashed arrows) at 10 Hz. Also, magnitude (solid arrow) and phase (θ) at 10 Hz are shown. With these baseline parameter values, the ε_2 component is zero and its locus is located at the origin, i.e., it contributes nothing to the overall complex stiffness. The overall complex stiffness is entirely a distortion stiffness and there is no recruitment component. *Right panel*, Force response of baseline sarcomeric model to step decrease in sarcomeric length. The separation of predominance of contributions by x_1 and x_2 components is clearly seen at ~ 10 ms. The response recovery for times < 10 ms is almost entirely due to the x_1 component and, for times > 10 ms, is almost entirely due to the x_2 component.

MATLAB was used to obtain polar graphs of Eqs. 11, 12, and 13 and, thus, polar graphs outputs of the x_1 , x_2 , and ε_2 components. Coefficient values in Eq. 13 were obtained from calculations according to Eqs. A47–A91 in the Appendix.

Under baseline conditions, at frequencies between 0.01 and 100 Hz, the polar locus of the x_1 component describes a truncated quasi-hemisphere in the first quadrant of the complex plane; the locus of the x_2 component describes a nearly complete quasi-hemisphere in the first quadrant; and the ε_2 component has no value at all. The x_1 and x_2 component polar loci are characteristic of high-pass filters. These differ in that the x_2 component passes lower frequencies than the x_1 component. The summation of components produces an overall complex stiffness that traverses a gull-winged locus tilted diagonally in the first quadrant of the complex plane (Fig. 2). At frequencies < 10 Hz, the x_2 component dominates to produce the arc of the left wing, and at frequencies > 10 Hz, frequency variation in the x_1 component dominates to produce the arc of the right wing. The dip in the locus between the two wings is the point where frequency-variation dominance is shifted from one component to the other. The sum of the x_1 and x_2 components is the total distortional stiffness.

There is no recruitment stiffness in the baseline model, and the plot does not go through the fourth quadrant. Because the stiffness locus is confined to the first quadrant, this baseline model exhibits only work-absorbing features and possess no work-producing features. The step response of the baseline model is shown in the right panel of Fig. 2. The recovery due to the x_1 component is, as expected, much faster (recovery from this component

is approximately 90% complete within 10 ms) than that from the x_2 component (approximately 90% complete in 250 ms).

Cooperatively coupled length responsiveness adds a band-pass filtering characteristic and a potential work-producing effect

The effect of RU–RU, XB–RU, and XB–XB cooperative mechanisms was evaluated by comparing the complex stiffness of the baseline condition to the complex stiffness when each type of cooperativity was introduced into the model at a high level by individually adjusting the parameters u , v , and w . RU–RU cooperativity simply amplified the distortional stiffness and did not introduce an ε_2 component or recruitment stiffness.

In contrast, both XB–RU and XB–XB cooperativities not only amplified the distortional stiffness but, also produced an ε_2 component, or recruitment stiffness. Of these two cooperativities, XB–XB cooperativity was much stronger in producing recruitment stiffness. The polar locus of this recruitment stiffness (Fig. 3) traversed a circular path beginning at the origin ($\omega = 0$), circling through the first quadrant, progressing on to enter the fourth quadrant at frequencies just above 1 Hz, where it continued until it entered the third quadrant at frequencies above 10 Hz. For all intents and purposes, the locus terminated at the origin at frequencies approaching 100 Hz. Such a locus is characteristic of a band-pass filter that attenuates low and high frequencies while passing only mid-range frequencies. The impact of a large ε_2 component on the shape of the $\varepsilon_m(j\omega)$ locus is dramatic. In this case, the ε_2 component adds to the distortional

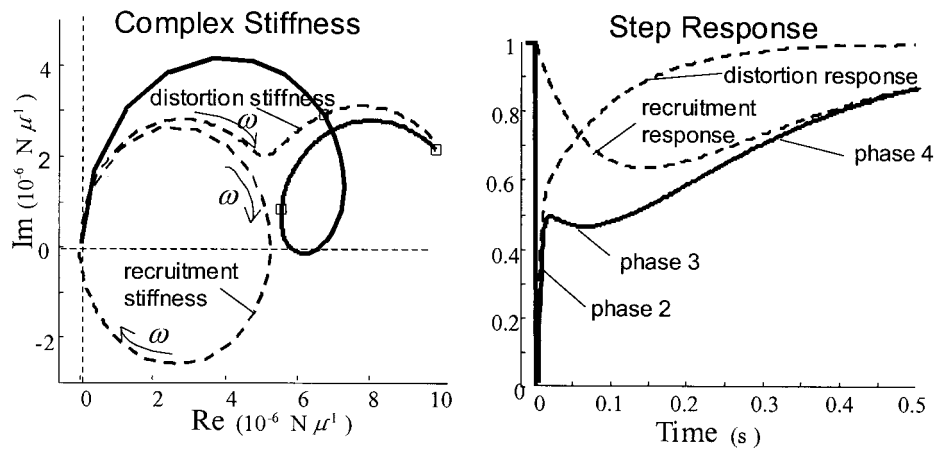


FIGURE 3 *Left panel*, Polar plot of overall complex stiffness (solid curve) for model expressing XB–XB cooperative behavior. This cooperativity gives rise to a significant recruitment stiffness (labeled dashed circle) that, when added to the distortion stiffness, imparts a looping aspect to the overall stiffness that dips into the fourth quadrant. *Right panel*, Force response of model (solid curve) to step change in sarcomeric length showing composition in terms of distortion and recruitment responses (dashed curves). The recruitment response contributes to the overall step response only after some time has passed, i.e., it is not immediate. The step response of a process with a band-pass filter dynamic is not sustained and slowly dies away.

stiffness to not only introduce a looping aspect to the $\varepsilon_m(j\omega)$ locus but also to cause the nadir of the locus to dip below the real axis into the fourth quadrant.

A fourth quadrant presence of $\varepsilon_m(j\omega)$ has profound physical meaning, i.e., for all frequencies in which $\varepsilon_m(j\omega)$ resides in the fourth quadrant (negative imaginary part and negative phase) the system behaves actively and performs positive cyclic work on its mechanical environment. This contrasts with first quadrant stiffness in which the system must absorb work from its mechanical environment to complete a cycle. Thus, the system behaves passively at frequencies where the stiffness locus resides in the first quadrant, i.e., when it has positive phase, but it behaves actively when the locus is in the fourth (and third) quadrant, i.e., when it has negative phase.

The corresponding step response is shown in the right panel of Fig. 3. The component of the step response due to recruitment stiffness develops relatively slowly and then recovers slowly to contribute a hump with long-lasting tail to the overall step response. Importantly, unlike the distortion stiffness response, the recruitment stiffness response is not immediate. It develops slowly and may be called delayed tension, a feature that has often been associated with the phenomenon of stretch activation (Pringle, 1978; Abbot and Steiger, 1977; Steiger, 1971).

It is of interest to compare the step response of Fig. 3 with the classic quick-release records obtained in frog sartorius muscle by Huxley and Simmons (1971). There are four phases identified in these classic records: phase 1 is the initial response coincident with the change in length; phase 2 is the fast recovery phase; phase 3 is the apparent plateau; and phase 4 is the slow recovery back toward the initial force. Each of these phases may be

identified in the model predicted response in Fig. 3. The segment of the model response corresponding to phase 3 can be made more or less pronounced by changing the strength of XB–XB cooperativity. Note that the time-duration of the various response segments may be easily altered to agree with the time durations seen in the Huxley–Simmons experiment by changing the kinetic constants in the myofilament model.

Structurally coupled length responsiveness adds a low-pass filtering characteristic and a significant positive work effect

There are two structurally coupled length-sensing mechanisms in the model: sliding filament mechanisms leading to changes in filament overlap (Eqs. A7–A11) and length-dependent XB attachment through the effect of β on the f - f' coefficient pair (Eqs. A16–A17). Both of these mechanisms generated an ε_2 component, or recruitment response, but the sliding filament effect from the ascending filament overlap region (Eq. A7) was very small. In contrast, the XB attachment effect could be made arbitrarily large by increasing the value of the parameter β . Importantly, the shape of the recruitment response locus from these structurally coupled length-responsiveness mechanisms was similar and differed fundamentally from the shape of the recruitment response locus resulting from cooperatively coupled mechanisms. In the case of structurally coupled length responsiveness, the recruitment stiffness locus began ($\omega = 0$) on the real axis away from the origin and traversed a half-circular path entirely below the real axis within the fourth quadrant for frequencies <10 Hz and, then, into the third quadrant for frequencies >10 Hz. For all intents and purposes, the locus

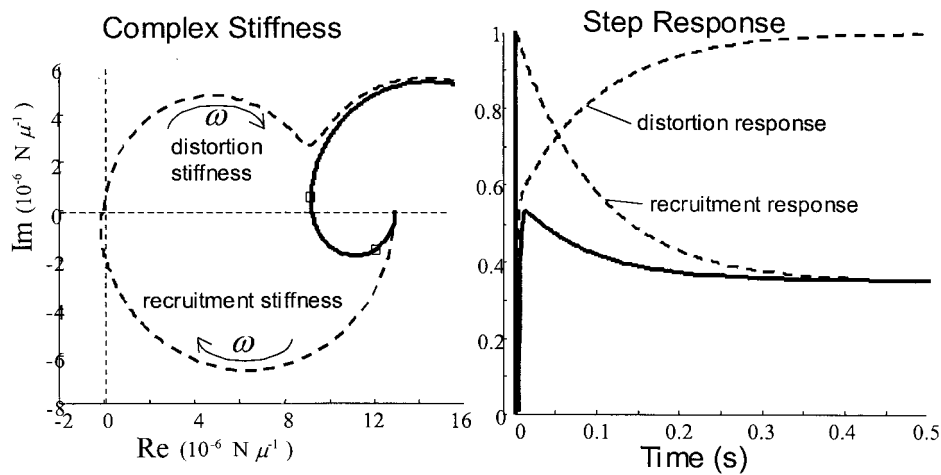


FIGURE 4 *Left panel*, Polar plot of overall complex stiffness (*solid curve*) for model expressing length-dependent XB attachment behavior. This form of structurally coupled length sensing gives rise to a large recruitment stiffness (*labeled dashed hemi-circle*) that, when added to the distortion stiffness, imparts an opening spiral form to the overall stiffness that begins and remains in the fourth quadrant as long as the recruitment stiffness dominates. *Right panel*, Force response of model (*solid curve*) with left panel complex stiffness to step change in sarcomeric length showing composition in terms of a distortion and recruitment responses (*dashed curves*). As with the example in Fig. 3, the recruitment response contributes to the overall step response only after some time has passed, i.e., it is not immediate. Different from recruitment due to cooperatively-coupled length responsiveness in Fig. 3, recruitment from structurally coupled length responsiveness persists and does not die away.

terminated at the origin at frequencies approaching 100 Hz. This locus is characteristic of a low pass filter.

When length-dependent XB attachment was given sufficient strength, the recruitment stiffness contributed significantly to $\varepsilon_m(j\omega)$ and dramatically changed the shape of its locus in the complex plane from the gull wing shape of the distortion stiffness to an opening spiral that began at a sizeable zero-frequency value on the real axis (Fig. 4). Importantly, the $\varepsilon_m(j\omega)$ locus began and remained in the fourth quadrant, where the recruitment stiffness dominated for most frequencies <10 Hz, before crossing into the first quadrant at higher frequencies, where the distortion stiffness dominated. For all frequencies where the locus was in the fourth quadrant, the sarcomere exhibited work-producing behavior.

The corresponding step response shown in the right panel of Fig. 4 demonstrates that the recruitment-stiffness response to a step change in length rises relatively slowly for a period and is then sustained. When added to the overall step response, this recruitment-stiffness response causes a slow depression after the initial fast recovery and a sustained depressed force. When seen as a response to a quick stretch, rather than to a quick release as in Fig. 4, this recruitment-stiffness response imparts a slow rise in force after the initial fast recovery and a sustained elevated force. Like the slowly developing force from the cooperatively coupled length responsiveness in Fig. 3, the slow developing force of structurally coupled length responsiveness is a delayed tension response and its sustained character is the sine qua non of stretch activation.

Structurally coupled plus cooperatively coupled length responsiveness add both a band-pass and a low-pass filtering characteristic

The $\varepsilon_m(j\omega)$ resulting from introducing both XB–XB cooperativity (cooperatively coupled length responsiveness) and length-dependent XB attachment (structurally coupled length responsiveness) into the model is shown in Fig. 5. The locus is characterized by four features: its zero frequency (or DC) value; a low-frequency first quadrant segment; a mid-frequency fourth quadrant segment; and a high-frequency first quadrant segment. The low-pass recruitment response from structurally coupled length responsiveness determines the zero frequency location of $\varepsilon_m(j\omega)$ on the real axis. Thereafter, at low frequencies, the band-pass recruitment stiffness from cooperatively coupled length responsiveness and the low-pass recruitment stiffness from structurally coupled length responsiveness mechanisms compete to determine the extent of the low frequency segment in the first quadrant. At frequencies where both the band-pass cooperatively coupled and low-pass structurally coupled recruitment stiffnesses reside in the fourth quadrant, these two stiffnesses work together and compete with the distortion stiffness to determine the extent of fourth quadrant looping. The recruitment stiffness from both structurally and cooperatively coupled length responses have decreasing influence on $\varepsilon_m(j\omega)$ as frequencies become high; high frequency $\varepsilon_m(j\omega)$ is determined almost exclusively by the distortion stiffness. These structurally and cooperatively coupled length responsiveness effects also combine in the step response to produce a delayed tension component,

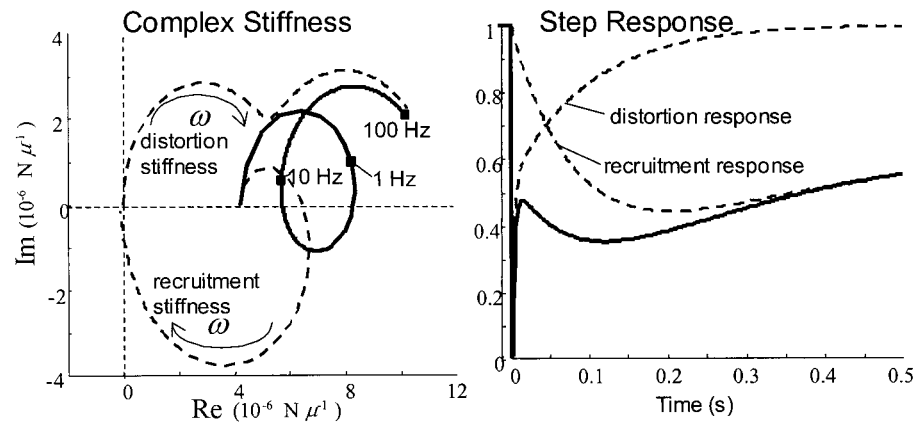


FIGURE 5 *Left panel*, Polar plot of overall complex stiffness (*solid curve*) for model expressing both cooperatively and structurally coupled forms of internal length-sensing behavior. In this case, the recruitment stiffness combines the features of the band-pass effect from cooperatively coupled length sensing and the low-pass effect from structurally coupled length sensing. The resulting looping locus of the overall stiffness possesses a significant fourth quadrant presence. *Right panel*, Force response of model (*solid curve*) with left panel complex stiffness to step change in sarcomeric length showing composition in terms of a distortion and recruitment responses (*dashed curves*). In this case, the recruitment response combines features of both cooperatively and structurally coupled length sensing with the result that it evolves apparently, more slowly than either of the two length sensing mechanisms by themselves.

part of which is not sustained and part of which is sustained, as one would expect, from the individual effects from the two recruitment mechanisms presented earlier.

Summary of myofilament model decomposition of sarcomeric stiffness

A nonlinear myofilament model was analyzed, according to steps summarized in Fig. 6, to predict the model's dynamic stiffness. This analysis led to a decomposition of stiffness into a component due to XB distortion and a component due to XB recruitment. The XB distortion component was due to

XB elastic properties and was scaled, but not altered dynamically, by recruitment effects. XB recruitment stiffness was induced by two classes of nonlinear phenomena: cooperatively-coupled length responsiveness as a result of XB-related cooperativities (i.e., XB–RU and XB–XB cooperativities only—other kinds of cooperativities did not induce a length-dependent dynamic recruitment effect); and, structurally-coupled length responsiveness as a result of changing filament overlap and length-dependent XB attachment step. Recruitment stiffness resulting from cooperatively coupled mechanisms could be characterized dynamically as a band-pass filter that introduced looping into the $\epsilon_m(j\omega)$

FIGURE 6 Steps in deriving stiffness predictions from a nonlinear myofilament model. This analysis naturally decomposes stiffness into distortional and recruitment components which are, in turn, made up of subcomponents as indicated in the figure and described in the text. Nonlinearities related to cooperativity and structural effects not only change the value of kinetic parameters but are also entirely responsible for the recruitment stiffness component.

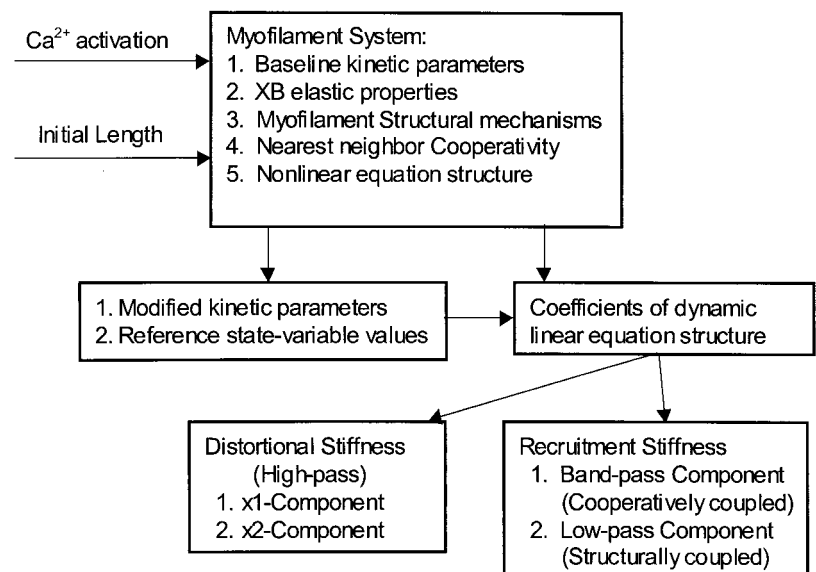
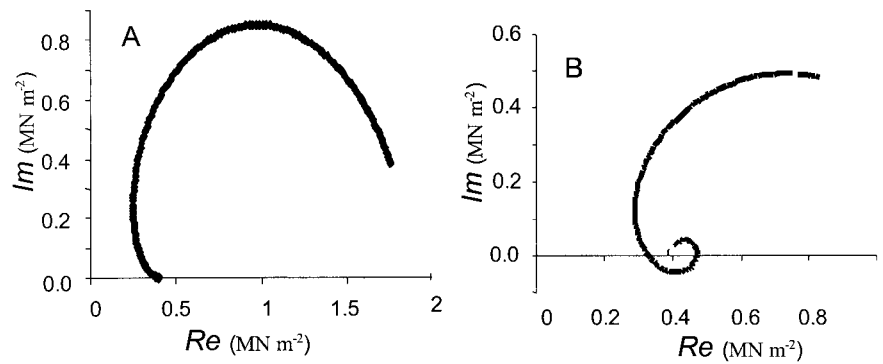


FIGURE 7 (A) Model reproduction of polar plots of cardiac muscle stiffness from the data of Wannenburg et al., (2000) obtained from the trabecular muscle of a rat. (B) Model reproduction of polar plots of cardiac muscle stiffness from the data of Blanchard et. al. (1999) obtained from the papillary muscle strip of a mouse. These two differing patterns of cardiac muscle stiffness are easily accommodated by the model. Units of stiffness are expressed in terms that are comparable to published data obtained experimentally. Myofilament parameters for both sets of data are given in Table 1.



locus. This looping could be sufficient to take the $\varepsilon_m(j\omega)$ locus into the fourth quadrant (positive work region) over a limited frequency range. This recruitment stiffness also produced a delayed tension effect in the step response that eventually died away. In contrast, recruitment stiffness resulting from structurally coupled mechanisms (i.e., length-dependent XB attachment) could be characterized dynamically as a low-pass filter that moved the zero frequency stiffness from the origin to the right along the real axis. Further, this effect caused the $\varepsilon_m(j\omega)$ locus to pass through the fourth quadrant (positive work region) at the lowest frequencies and produced a delayed tension effect in the step response that was sustained. Both band-pass and low-pass recruitment mechanisms participate in the stretch activation phenomenon.

REPRODUCTION AND INTERPRETATION OF EXPERIMENTAL DATA FROM CARDIAC MUSCLE WITH THE MYOFILAMENT MODEL

To adapt the generic distortion-recruitment model to cardiac muscle, myofilament kinetic parameters were adjusted to reproduce as closely as possible the best-fit complex stiffness locus of data obtained from rat trabecular cardiac muscle (Wannenburg et al., 2000) and from mouse LV papillary muscle (Blanchard et al., 1999). These two sets of data differed in that the Wannenburg data had no detectable first quadrant looping at the lowest frequencies and no obvious fourth quadrant presence, whereas the Blanchard data had both first quadrant looping at the lowest frequencies and significant low-frequency fourth quadrant presence. These data sets were selected for reproduction because they represent extremes of the more common observation that cardiac muscle stiffness exhibits a low-frequency fourth quadrant presence but not low-frequency first quadrant looping (Berman et al., 1988; Saeki et al., 1991; Kawai et al., 1993; Rossmann et al., 1986; Shibata et al., 1987; Campbell et al., 1993). Fitting to the selected data was by adjusting model parameters with a least squares optimizer to minimize the difference between the model-

predicted polar locus and each of the polar loci reported by respective authors. The resulting polar plot reproductions are given in Fig. 7 and the corresponding cardiac myofilament parameters for each set of data are given in Table 1. The model-generated polar plot loci given in Fig. 7 are virtually indistinguishable from the curves given by the authors in the original publications. Although, because many parameters were allowed to undergo change, the parameters estimated by our curve-fitting technique and reported in Table 1 are not unique, they may be taken as starting points for the current comparison and for future evaluations of cardiac muscle mechanodynamics.

Note that XB cycle kinetic parameters (f, f', h, h', g) in the mouse are larger than the corresponding parameters in the rat (Table 1) as one would expect for muscle from a heart that beats at 500–600 min^{-1} as opposed to muscle from a heart that beats at 200–300 min^{-1} . However, the relative values among XB kinetic parameters within a species is about the same, with a surprisingly high value of f' relative to f in both species. This indicated that the A_1 (prepower stroke) state was underpopulated relative to the A_2 and D states in both species. A second item of interest is that the nonlinear phenomena associated with cooperativity and length-dependent XB attachment are present in apparently equal strengths in both species. However, the fact that the stiffness polar loci are so different for these two sets of model parameters indicates that only subtle differences in the nonlinear parameters are sufficient to produce polar loci that appear quite different.

DISTORTION-RECRUITMENT INTERPRETATION OF MUSCLE STIFFNESS DIFFERS FROM PREVAILING VIEW

The distortion-recruitment interpretive framework presented above leads to a different understanding of processes responsible for dynamic muscle stiffness than would be obtained using the prevailing view. The prevailing view decomposes muscle stiffness into four first-order high-pass

filters often referred to as the A, B, C, and D processes, as in

$$\varepsilon_m(j\omega) = H_0 + A \frac{j\omega}{j\omega + a} - B \frac{j\omega}{j\omega + b} + C \frac{j\omega}{j\omega + c} + D \frac{j\omega}{j\omega + d}. \quad (15)$$

This prevailing view was first put forth by Kawai and Brandt (1980) as the sum of three filters representing the A, B, and C processes and then expanded to four filters by Kawai et al. (1993) and Zhao and Kawai (1993), who added the D process.

The characteristic frequency of each filter bears a putative relationship to a specific step in the XB cycle. A basic assumption in assigning these relations is that there is at least an order of magnitude difference in the XB kinetic constants, such that each kinetic step may exhibit dynamically as an uncontaminated mechanodynamic event. In this prevailing view, recruitment and distortion are not recognized explicitly as phenomena that contribute to stiffness. Further, there is no means by which mechanisms such as cooperativity and explicit length sensing can participate in stiffness dynamics. In the prevailing view, all fourth quadrant presence of the stiffness locus derives from the negative sign on the B process, which is assigned because the B process putatively derives from the active force-generating isomerization step (power stroke) in the XB cycle.

In contrast, the distortion-recruitment theory divides stiffness dynamics into x_1 - and x_2 -distortional components that act as high-pass filters and a recruitment component that may appear in the form of a low-pass filter, a band-pass filter, or a combination of low-pass and band-pass filters. Important to the distortion-recruitment theory, is that recruitment dynamics arise from nonlinearities in the myofilament kinetic system. These act to give rise to internal length sensing by the myofilament system and are entirely responsible for any fourth quadrant presence in the $\varepsilon_m(j\omega)$ polar locus. As demonstrated in Fig. 2, the power stroke in the XB cycle cannot, by itself, be responsible for fourth quadrant stiffness and cannot give rise to positive work features of constantly activated muscle. Although not sufficient, the power stroke is necessary for any positive work feature, as can be seen in Eq. 14, where it is shown that recruitment stiffness is the product of the outcome of the powerstroke, x_0 , and $H_{e_2}(j\omega)$. Thus, if there is no power stroke, there is no x_0 and no recruitment stiffness and, consequently, no positive work.

Another important feature of the distortion-recruitment theory comes from inspection of the $H_y(j\omega)$, which demonstrates that there is considerable complexity in relationships between myofilament kinetic events and dynamic coefficients associated with both distortion and recruitment. There is no correspondence between any single dynamic

characteristic and a single myofilament kinetic step; each dynamic characteristic depends on multiple underlying kinetic features of the myofilament system. With these fundamental differences, interpretations based on the prevailing-view model lead to very different understanding of mechanisms responsible for muscle stiffness than would be obtained from the interpretations based on the distortion-recruitment model presented here.

Clearly, there is a need to simplify the distortion-recruitment theory if it is to find application either for simulation or identification purposes. As a beginning point for reduced representation, we suggest the following approximations. The numerator and denominator polynomials of the transfer functions, ($H_{x_1}(j\omega)$, $H_{x_2}(j\omega)$, and $H_{e_2}(j\omega)$) in Eqs. 11–13, may be factored into terms containing the polynomial roots. Roots of numerator polynomials are designated as zeros, and roots of the denominator polynomial are designated as poles. The zero of the single factor in the numerator of $H_{x_1}(j\omega)$ of Eq. 11 approximately cancels the lowest valued pole of the two-factor representation of the denominator polynomial. In contrast, the zero of the single factor in the numerator of $H_{x_2}(j\omega)$ of Eq. 12 approximately cancels the highest valued pole of the two-factor representation of the denominator polynomial. As a consequence, the two components of distortional stiffness may be taken as approximately independent and may be written as

$$x_1 \text{ component} = E_1 \frac{j\omega}{j\omega + d_1}, \quad (16)$$

$$x_2 \text{ component} = E_2 \frac{j\omega}{j\omega + d_2}, \quad (17)$$

where E_1 and E_2 are magnitude scaling parameters and d_1 and d_2 are dynamic parameters for the respective processes. These reduced formulations retain the essential high-pass filtering characteristics of the original formulations.

A second approximation is that one of the three roots of the denominator polynomial of Eq. 13 is of much larger magnitude than the other two, such that the large-magnitude root contributes little to dynamics at frequencies of interest. After dropping the large-magnitude root, the following further simplifications may be taken without any appreciable loss of fidelity

$$\text{band-pass recruitment stiffness} = R_{\text{coop}} \frac{j\omega/(j\omega + a)}{(j\omega)^2 + 2\zeta\omega_n(j\omega) + \omega_n^2}, \quad (18)$$

$$\text{low-pass recruitment stiffness} = R_{\text{str}} \frac{b}{(j\omega)^2 + 2\zeta\omega_n(j\omega) + \omega_n^2}, \quad (19)$$

where R_{coop} and R_{str} are magnitude scaling parameters for the cooperatively based band-pass recruitment stiffness and

structurally based, low-pass recruitment stiffness respectively. Further, a , b , ζ , and ω_n are dynamic parameters for the respective processes. Eq. 18 retains the band-pass filtering characteristics of the original expression for cooperatively coupled recruitment stiffness, and Eq. 19 retains the low-pass filtering characteristics of the original expression for structurally coupled recruitment stiffness. Eqs. 16–19 represent simplified, reduced versions of the distortion-recruitment model that emphasize system-dynamic parameters rather than myofilament-kinetic parameters. The nine parameters in Eqs. 16–19 are no more than the nine parameters in the prevailing view formulation, Eq. 15, and many fewer than the eighteen parameters in the linearized model equations, Eqs. 9–13. In the reduced version of the distortion-recruitment model, there remains explicit representation of basic myofilament phenomena such as cooperativity (band-pass recruitment stiffness), but there is no attempt to relate these representations to specific kinetic steps.

Further reductions may be made for cardiac muscle in that many authors report no observable first quadrant looping in cardiac muscle at the lowest frequencies (Berman et al., 1988; Saeki et al., 1991; Kawai et al., 1993; Rossmanith et al., 1986; Shibata et al., 1987; Campbell et al., 1993; Wannenburg et al., 2000) suggesting no role for the prevailing model's A process. Additionally, frequencies of the D process appear to be above those of physiological interest. This has led to the practice of using just a five-parameter version of the prevailing-view model to fit cardiac muscle stiffness data,

$$\varepsilon_m(j\omega) = H_0 - B \frac{j\omega}{j\omega + b} + C \frac{j\omega}{j\omega + c}. \quad (20)$$

This reduced form is equivalent to a six-parameter reduced version of the distortion-recruitment model,

$$\varepsilon_m(j\omega) = E_1 \frac{j\omega}{j\omega + d} + R_{\text{rec}} \left\{ \frac{[j\omega/(j\omega + d)] + b}{(j\omega)^2 + 2\zeta\omega_n(j\omega) + \omega_n^2} \right\}, \quad (21)$$

which may be reduced even further to a five-parameter version under circumstances where one of the poles in the denominator of the recruitment term is far to the left. Some complex stiffness loci can be fit equally well with both of these formulations. However, the parameters obtained with each will give quite different interpretations. In the prevailing view of Eq. 20, the time constant associated with the B process has a putative relation to the XB attachment (and powerstroke) step, while that associated with the C process has a putative relation to the XB detachment step. In the reduced distortion-recruitment model, all distortional dynamics are captured in the first term on the right-hand side and all recruitment dynamics are captured in the second term. For this reduced model, the parameter interpretations are as follows: E_1 , instantaneous stiffness that is propor-

tional to the number of attached XB; d , a characteristic frequency by which distorted XB are replaced by undistorted XB; $R_{\text{rec}}b/\omega_n^2$, zero frequency stiffness equal to the slope of steady-state length-tension relationship; ζ , damping within the recruitment process expressing the tendency for oscillations; and ω_n , characteristic frequency for recruitment processes, which expresses the combined effect of all kinetic coefficients in the myofilament kinetic scheme.

A rough mapping between parameters in the prevailing-view and distortion-recruitment models may be made as follows. Parameters C and c in the prevailing-view model are roughly equal in value to parameters E_1 and d in the distortion-recruitment model. Parameter B in the prevailing-view model is roughly equal in value to R_{rec} in the distortion-recruitment model and parameter b in the prevailing view model has some equivalence to the smaller of the two roots of the denominator polynomial, $(j\omega)^2 + 2\zeta\omega_n(j\omega) + \omega_n^2$, in the distortion recruitment model. However, when estimated from stiffness data obtained in isolated cardiac muscle, the interpretations assigned to these analogous-valued parameters will be substantially different. We claim that the parameters of the reduced distortion-recruitment model are not only characteristic of observed stiffness dynamics but, also, give a new sense of appreciation for the underlying contractile processes responsible for these dynamics.

OVERALL SUMMARY

A myofilament model of sarcomeric stiffness based on distortion and recruitment concepts not only accurately reproduces every feature of experimentally measured cardiac muscle stiffness, but also provides a novel basis for interpretation of these features in terms of underlying nonlinear contractile mechanisms. Through this interpretive framework, cardiac muscle stiffness provides a window to contractile processes and a unique context in which to relate elemental sarcomeric processes to the functional behaviors of different muscle types or altered states (e.g., disease) within a given muscle type.

APPENDIX

This Appendix lists the relevant mathematical expressions of the model and its predictions as given in the text. Developments of these equations have been presented in preliminary form in Razumova et al. (1999, 2000) and Campbell et al. (2001).

Dynamic equation list

State variable differential equations

Model state variables may be divided between recruitment variables (i.e., the numbers of XB in the D, A_1 , and A_2 states in the XB cycling scheme of Fig. 1) and distortional variables (i.e., the average distortion of all XB in the A_1 and A_2 states). The state variable differential equations describing

rates of changes of recruitment variables can be written from inspection of Fig. 1 as

$$\dot{D}(t) = k_{\text{on}}R_{\text{off}}(t) + f'A_1(t) + gA_2(t) - [k_{\text{off}} + f]D(t) \quad (\text{A1})$$

$$\dot{A}_1(t) = fD(t) + h'A_2(t) - [f' + h]A_1(t) \quad (\text{A2})$$

$$\dot{A}_2(t) = hA_1(t) - [h' + g]A_2(t) \quad (\text{A3})$$

It is understood in Eqs. A1–A3 that the kinetic coefficients k_{on} , k_{off} , f , f' , h , h' , and g are not constants and depend on state variables and input variables according to relations given below.

The state variable differential equations for the x_1 and x_2 distortional variables are derived according to the following. Let $x_1(t)$ be the time-varying average distortion among A_1 XB and $x_2(t)$ be the time-varying average distortion among A_2 XB. There are two phenomena causing distortion of XB: chemomechanical energy transduction during the XB power stroke causing elastic energy storage in the XB as transition is made from state A_1 to state A_2 , and shearing between filaments during sliding between thick and thin filaments when sarcomere length, L_S , changes. These two phenomena are treated as independent.

Independent distortional effects are seen in the development of the differential equation for $x_2(t)$. This derivation uses a macroscopic distortion balance over all parallel XB in the A_2 state in the half sarcomere. The collective distortion among the parallel A_2 XB is given by

$$X_2(t) = A_2(t)x_2(t) \quad (\text{A3a})$$

where the upper case $X_2(t)$ is used to designate the collective distortion and the small case, $x_2(t)$, designates the average distortion among the $A_2(t)$ XB. $X_2(t)$ at some $t + \Delta t$, can be written as

$$\begin{aligned} X_2(t + \Delta t) = X_2(t) &+ \left[\text{added distortion due to shear} \right. \\ &\left. \text{from change in } L_S \text{ over } \Delta t \right] \\ &+ \left[\text{added distortion due to formation of} \right. \\ &\left. \text{new } A_2 \text{ XB via power stroke over } \Delta t \right] \\ &- \left[\text{lost distortion due to transition of} \right. \\ &\left. \text{distorted } A_2 \text{ XB to other states over } \Delta t \right] \end{aligned} \quad (\text{A3b})$$

where

$$\begin{aligned} &[\text{added distortion due to shear from change in } L_S \text{ over } \Delta t] \\ &= \left[\begin{array}{l} \text{(externally imposed } \Delta L_S/2) \\ \text{(\#} A_2 \text{ XB existent at } t) \end{array} \right] = (\Delta L_S/2)A_2(t) \end{aligned} \quad (\text{A3c})$$

$$\begin{aligned} &[\text{added distortion due to formation of new } A_2 \text{ XB over } \Delta t] \\ &= \left[\begin{array}{l} \text{(number of newly formed } A_2 \text{ XB)} \\ \text{distortion of newly formed XB} \end{array} \right] \\ &= [hA_1(t)]\Delta t(x_0 + x_1 + \Delta L_S/4) \end{aligned} \quad (\text{A3d})$$

[lost distortion due to transition of distorted A_2 XB to other states over Δt]

$$\begin{aligned} &= \left[\begin{array}{l} \text{(number of } A_2 \text{ XB lost)} \\ \text{(average distortion of these lost } A_2 \text{ XB)} \end{array} \right] \\ &= [(g + h')A_2(t)]\Delta tx_2(t) \end{aligned} \quad (\text{A3e})$$

The power stroke induces, on the average, x_0 distortion in XB as they enter the A_2 state from the A_1 state. In addition, because we treat distortion from the power stroke and that from sliding filaments as independent events, the XB entering the A_2 state bring with them whatever distortion they may have possessed in the A_1 state prior to the transition to A_2 .

Substituting Eqs. A3c–A3e into Eq. A3b gives

$$\begin{aligned} X_2(t + \Delta t) = X_2(t) &+ \frac{\Delta L_S}{2} A_2(t) \\ &+ [hA_1(t)]\Delta t \left(x_0 + x_1 + \frac{\Delta L_S}{4} \right) \\ &- [(g + h')A_2(t)]\Delta tx_2(t) \end{aligned} \quad (\text{A3f})$$

Rearranging,

$$\begin{aligned} \frac{X_2(t + \Delta t) - X_2(t)}{\Delta t} &= A_2(t) \frac{\Delta L_S}{2\Delta t} + [hA_1(t)] \left(x_0 + x_1 + \frac{\Delta L_S}{4} \right) \\ &- [(g + h')A_2(t)]x_2(t) \end{aligned} \quad (\text{A3g})$$

Taking the limit as $\Delta t \rightarrow 0$, yields

$$\begin{aligned} \dot{X}_2(t) = A_2(t) \frac{\dot{L}_S}{2} &+ [hA_1(t)][x_0 + x_1] \\ &- (g + h')A_2(t)x_2(t) \end{aligned} \quad (\text{A3h})$$

Now, $\dot{X}_2(t)$ may be eliminated from Eq. A3h by noting that differentiation of Eq. A3g yields

$$\dot{X}_2(t) = \dot{A}_2(t)x_2(t) + A_2(t)\dot{x}_2(t) \quad (\text{A3i})$$

Equating Eqs. A3h and A3i, making appropriate substitutions for $\dot{A}_2(t)$ from Eq. A3, and solving for $\dot{x}_2(t)$, gives the desired differential equation,

$$\dot{x}_2(t) = -h \frac{A_1(t)}{A_2(t)} [x_2(t) - (x_1(t) + x_0)] + \frac{\dot{L}_S(t)}{2} \quad (\text{A4})$$

In like manner, it can be shown that

$$\begin{aligned} \dot{x}_1(t) = - \left[f \frac{D(t)}{A_1(t)} + h' \frac{A_2(t)}{A_1(t)} \right] x_1(t) &+ h' \frac{A_2(t)}{A_1(t)} [x_2(t) - x_0] \\ &+ \frac{\dot{L}_S(t)}{2} \end{aligned} \quad (\text{A5})$$

where XB enter the A_1 state from D with no distortion, but return to A_1 from A_2 via the reverse power stroke with residual distortion not removed by loss of x_0 .

Output equation

The model is structured such that it may be viewed as being driven by two input signals: the time course of available activator calcium, $Ca(t)$, and the time course of sarcomere length, L_S . The model responds with a single output, the predicted force, $F(t)$. Force prediction is given by the model output equation (Razumova et al., 1999),

$$F(t) = \eta A_1(t)x_1(t) + \eta A_2(t)x_2(t) \quad (\text{A6})$$

Nonlinear phenomena in myofibril system

Filament overlap. Let Z be the length of the overlap region of thick and thin filaments in a half sarcomere that allow cycling XB. Also, let L_A = length of thin filament, L_M = length of thick filament, and B = length of thick filament bare zone. Then,

$$\text{If } L_S < 2L_A - B, \text{ then } Z = \frac{1}{2}L_S + [L_M/2 - L_A] \quad (\text{A7})$$

$$\text{If } 2L_A - B < L_S < 2L_A + B, \text{ then } Z = \frac{1}{2}[L_M - B] \quad (\text{A8})$$

$$\text{If } L_S > 2L_A + B, \text{ then } Z = -\frac{1}{2}L_S + [L_M/2 + L_A] \quad (\text{A9})$$

Let R_T equal the number of XB in a half sarcomere and R_Z equal the number of XB in the Z overlap region. Then,

$$R_Z = \frac{Z}{\frac{1}{2}[L_M - B]} R_T \quad (\text{A10})$$

$$R_{\text{off}} = R_Z - D - A_1 - A_2 \quad (\text{A11})$$

Saturation effects from Ca^{2+} -binding Isotherms. For a single low-affinity Ca^{2+} -binding site to TnC, as in cardiac muscle, the binding isotherm is

$$[\text{binding isotherm}]_1 = \frac{\text{Ca}(t)}{K_1 + \text{Ca}(t)} \quad (\text{A12})$$

where K_1 is the half saturation concentration for binding to the available site. For two low-affinity Ca^{2+} -binding sites on TnC, as in fast skeletal muscle, the binding isotherm is

$$[\text{binding isotherm}]_2 = \frac{\text{Ca}(t)^2}{K_1 K_2 + K_2 \text{Ca}(t) + \text{Ca}(t)^2} \quad (\text{A13})$$

where K_1 and K_2 are the half saturation concentrations for binding to the first and second sites, respectively.

Input variable-dependent coefficients. Calcium-dependent RU on-off coefficients. For any level of Ca^{2+} -binding, the reference value of the RU on-off coefficients are given by

$$k_{\text{on}}^{\text{ref}} = k_{\text{on}}^0 + (k_{\text{on}}^{\text{Ca}} - k_{\text{on}}^0)[\text{binding isotherm}] \quad (\text{A14})$$

$$k_{\text{off}}^{\text{ref}} = k_{\text{off}}^0 + (k_{\text{off}}^{\text{Ca}} - k_{\text{off}}^0)[\text{binding isotherm}] \quad (\text{A15})$$

where the 0 superscript indicates the value of the coefficient when Ca^{2+} is not bound to TnC, and the Ca superscript indicates the value when the TnC binding site is saturated.

Sarcomere length-dependent attachment coefficient. In our conception, changes in L_S causes changes in longitudinal and transverse dimensions of the myofibril system. Longitudinal dimension changes are responsible for changing filament overlap as described above; transverse dimension changes are responsible for changes in transverse interfilament spacing. Increases in L_S causes decreases in interfilament lattice spacing and reduces the distance that the myosin head must travel to attach to the actin-binding site and, thus, reduces the activation energy barrier for XB attachment (Godt and Maughan, 1981; McDonald and Moss, 1995; Fuchs and Smith, 2001). The result is that the probability for myosin attachment to actin increases. For this reason, we changed the f_2' coefficient pair with changes in L_S because these coefficients govern the attachment step in our XB scheme. We had no rationale for

changing h , h' , and g with sarcomere length and, therefore, we did not allow these coefficients to be length sensitive.

To consider the impact of L_S on D-to- A_1 transitions, we defined a normalized L_S variable as

$$\chi = \frac{L_S - L_{S0}}{L_{S0}}$$

where L_{S0} is a reference L_S . Let decreased lattice spacing due to increased L_S reduce the activation energy, B , needed for a D-to- A_1 transition as

$$B_{D A_1} = B_{D A_1}^0 - b\chi$$

where b is a coefficient expressing the strength of the activation energy reduction, and the 0 superscript on B refers the first term on the right-hand side to the activation energy at $L_S = L_{S0}$. Then, according to normal activation energy conventions, the rate coefficient for a D-to- A_1 transition is enhanced with χ according to

$$f_{LS} = f_a [e^{-B_{D A_1}^0 - b\chi / \kappa T}] = f_0 [e^{\beta \chi}] \quad (\text{A16})$$

where f_{LS} is the value of f due to just L_S effects, f_a is an attempt frequency, β equals $b/\kappa T$, and f_0 is the coefficient governing D-to- A_1 transition at L_{S0} . Coincidentally, following normal conventions, the probability for an A_1 -to-D transition is reduced with increased L_S according to

$$f'_{LS} = f'_a [e^{-(B_{A D}^0 - b\chi) / \kappa T}] = f'_0 [e^{-\beta \chi}] \quad (\text{A17})$$

The outcome from this treatment of the effect of L_S on the kinetics of the attachment step is that the strength of these effects in the model can be graded with the single parameter, β .

State variable-dependent coefficients. Neighbor Interactions. Considering three kinds of nearest-neighbor interactions (RU-RU, XB-RU, and XB-XB interactions), we grade the strength of each of these interactions with the parameters: u , w , and v , respectively. Then, combining the independent effects of each interaction, as developed and presented in Razumova et. al. (2000) as single terms, these interaction effects may be represented as

$$k_{\text{on}} = k_{\text{on}}^{\text{ref}} \left[1 + \frac{D}{R_Z} (u - 1) + \frac{A_1}{R_Z} (ue^{(w-1)(x_1/x_0)} - 1) + \frac{A_2}{R_Z} (ue^{(w-1)(x_2/x_0)} - 1) \right]^2 \quad (\text{A18})$$

$$k_{\text{off}} = k_{\text{off}}^{\text{ref}} \left[1 + \frac{D}{R_Z} \left(\frac{1}{u} - 1 \right) + \frac{A_1}{R_Z} \left(\frac{e^{-(w-1)(x_2/x_0)}}{u} - 1 \right) + \frac{A_2}{R_Z} \left(\frac{e^{-(w-1)(x_2/x_0)}}{u} - 1 \right) \right]^2 \quad (\text{A19})$$

$$f = f_{LS} \left[1 + \frac{A_1}{R_Z} (e^{(v-1)(x_1/x_0)} - 1) + \frac{A_2}{R_Z} (e^{(v-1)(x_2/x_0)} - 1) \right]^2 \quad (\text{A20})$$

$$f' = f'_{LS} \left[1 + \frac{A_1}{R_Z} (e^{-(v-1)(x_1/x_0)} - 1) + \frac{A_2}{R_Z} (e^{-(v-1)(x_2/x_0)} - 1) \right]^2 \quad (\text{A21})$$

where $k_{\text{on}}^{\text{ref}}$ and $k_{\text{off}}^{\text{ref}}$ refer to baseline values of the respective coefficients when there are no nearest-neighbor cooperative effects.

Distortion-dependent kinetic coefficients. A central tenet in XB theory is that kinetic coefficients leading away from attached states must change according to the elastic energy stored in those states due to elastic deformation (i.e., distortion). Because elastic energy changes with the square of elastic deformation, it may be argued that these kinetic coefficient changes are nearly parabolic around an isometric reference state. If so, there will be no appreciable changes in these coefficients for small amplitude length perturbations, and this allows distortion dependence to be ignored (Thorson and White, 1983).

Steady-state equations

All variations arising from small-amplitude-length perturbations take place around a steady-state, isometric baseline. Because of nonlinearities, the baseline state influences small-amplitude dynamic behavior. Thus, solution of the steady-state model to determine baseline values is required before dynamic behavior can be determined.

Under steady-state isometric conditions all inputs are constant, i.e., $L_S(t) = L_{S0}$ and $\text{Ca}(t) = \text{Ca}_0$. Thus, the differential equations become algebraic equations and the steady-state equation list may be restructured into Eqs. A7–A17 plus the following set of seven simultaneous algebraic equations.

$$k_{\text{on}} = k_{\text{on}}^{\text{ref}} \left[1 + \frac{D_0 + A_{10}}{R_Z} (u - 1) + \frac{A_{20}}{R_Z} (ue^{(w-1)} - 1) \right]^2 \quad (\text{A22})$$

$$k_{\text{off}} = k_{\text{off}}^{\text{ref}} \left[1 + \frac{D_0 + A_{10}}{R_Z} \left(\frac{1}{u} - 1 \right) + \frac{A_{20}}{R_Z} \left(\frac{1}{ue^{(w-1)}} - 1 \right) \right]^2 \quad (\text{A23})$$

$$f = f_{\text{LS}} \left[1 + \frac{A_{20}}{R_Z} (e^{(v-1)} - 1) \right]^2 \quad (\text{A24})$$

$$f' = f'_{\text{LS}} \left[1 + \frac{A_{20}}{R_Z} \left(\frac{1}{e^{(v-1)}} - 1 \right) \right]^2 \quad (\text{A25})$$

$$D = \frac{k_{\text{on}}}{k_{\text{on}} + k_{\text{off}} + f} R_Z + \frac{f' - k_{\text{on}}}{k_{\text{on}} + k_{\text{off}} + f} A_1 + \frac{g - k_{\text{on}}}{k_{\text{on}} + k_{\text{off}} + f} A_2 \quad (\text{A26})$$

$$A_1 = \frac{f}{f' + h} D + \frac{h'}{f' + h} A_2 \quad (\text{A27})$$

$$A_2 = \frac{h}{h' + g} A_1 \quad (\text{A28})$$

Under isometric conditions, $x_1 = 0$ and $x_2 = x_0$, and the output equation reduces to

$$F = \eta A_2 x_0 \quad (\text{A29})$$

Model linearization

Once steady-state values were determined, small-amplitude model behavior is given by the model's linearized dynamic equations. The nonlinear, state-variable, differential Eqs. A1–A5 were linearized by taking a first-order Taylor expansion about the reference state to create a set of linear differential equations. Let the i indexed upper case Y_i , represent state variables (A_1, A_2, D, x_1, x_2) and the m indexed upper-case, U_m , represent input variables (L_S, Ca). Thus, $i = 1, 2, 3, 4, 5$ and $m = 1, 2$. The indexed lower-case y_i and u_m represent respective incremental deviations of state variables and input variables from their reference values. Index values are assigned according to

$$y_1 = A_1 - A_{10}, \quad y_2 = A_2 - A_{20}, \quad y_3 = D - D_0$$

$$y_4 = x_1 - x_{10}, \quad y_5 = x_2 - x_{20}$$

$$u_1 = \text{Ca} - \text{Ca}_0, \quad u_2 = L_S - L_{S0}$$

where the subscript 0 represents the reference value. The general form for linearized differential equations is given by

$$\dot{y}_i = \sum_j \partial_i^{Y_j} y_j + \sum_m \partial_i^{U_m} u_m \quad (\text{A30})$$

where the $\partial_i^{Y_j}$ are the values of the partial derivatives of the Y_i with respect to the Y_j ($j = 1, 2, 3, 4, 5$) evaluated at the reference state, and the $\partial_i^{U_m}$ are the values of the partial derivatives of the Y_i with respect to the U_m also evaluated at the reference state.

Once the $\partial_i^{Y_j}$ and $\partial_i^{U_m}$ are known, the linear differential equations for incremental variation around the reference state may be written from Eqs. A1–A5 as

$$\dot{y}_1 = \partial_1^1 y_1 + \partial_1^2 y_2 + \partial_1^3 y_3 + \partial_1^4 y_4 + \partial_1^5 y_5 + \partial_1^{u_2} u_2 \quad (\text{A31})$$

$$\dot{y}_2 = \partial_2^1 y_1 + \partial_2^2 y_2 \quad (\text{A32})$$

$$\dot{y}_3 = \partial_3^1 y_1 + \partial_3^2 y_2 + \partial_3^3 y_3 + \partial_3^4 y_4 + \partial_3^5 y_5 + \partial_3^{u_1} u_1 + \partial_3^{u_2} u_2 \quad (\text{A33})$$

$$\dot{y}_4 = \partial_4^4 y_4 + \partial_4^5 y_5 + \partial_4^{u_3} u_2 \quad (\text{A34})$$

$$\dot{y}_5 = \partial_5^4 y_4 + \partial_5^5 y_5 + \partial_5^{u_3} u_2 \quad (\text{A35})$$

That there are different numbers of terms on the right-hand side of these equations is because the values of particular partial derivatives were zero, i.e., there was no dependence of the respective time derivative on the variable of the partial derivative. These zero-valued terms were dropped from Eqs. A31–A35. The linearized differential Eqs. A31–A35, were Fourier transformed to produce the set of simultaneous algebraic equations in the complex frequency ($j\omega$) domain,

$$j\omega y_1 = \partial_1^1 y_1 + \partial_1^2 y_2 + \partial_1^3 y_3 + \partial_1^4 y_4 + \partial_1^5 y_5 + \partial_1^{u_2} u_2 \quad (\text{A36})$$

$$j\omega y_2 = \partial_2^1 y_1 + \partial_2^2 y_2 \quad (\text{A37})$$

$$j\omega y_3 = \partial_3^1 y_1 + \partial_3^2 y_2 + \partial_3^3 y_3 + \partial_3^4 y_4 + \partial_3^5 y_5 + \partial_3^{u_1} u_1 + \partial_3^{u_2} u_2 \quad (\text{A38})$$

$$j\omega y_4 = \partial_4^4 y_4 + \partial_4^5 y_5 + \partial_4^{u_3} j\omega u_2 \quad (\text{A39})$$

$$j\omega y_5 = \partial_5^4 y_4 + \partial_5^5 y_5 + \partial_5^{u_3} j\omega u_2 \quad (\text{A40})$$

where the y_i , as frequency transformed variables, are now functions of complex frequency rather than functions of time as in the differential Eqs. A31–A35.

Now, the overall complex stiffness was defined in the text in terms of three components as

$$\underbrace{\frac{dF}{dL_S}(j\omega)}_{\text{sarcomeric stiffness}} = \underbrace{\frac{\varepsilon_{10}H_{x_1}(j\omega)}{x_1 \text{ component}} + \frac{\varepsilon_{20}H_{x_2}(j\omega)}{x_2 \text{ component}}}_{\text{distortion stiffness}} + \underbrace{\frac{x_0H_{\varepsilon_2}(j\omega)}{\varepsilon_2 \text{ component}}}_{\text{recruitment stiffness}} \quad (\text{A41})$$

Recognizing that $u_2 = dL_S$, each of the frequency-dependent transfer functions within each component was identified as

$$H_{x_1}(j\omega) = \frac{y_4}{u_2}(j\omega) \quad (\text{A42})$$

where y_4 is the frequency-domain representation of the incremental variation in $x_1(t)$;

$$H_{x_2}(j\omega) = \frac{y_5}{u_2}(j\omega) \quad (\text{A43})$$

where y_5 is the frequency-domain representation of the incremental variation in $x_2(t)$; and

$$H_{\varepsilon_2}(j\omega) = \frac{y_2}{u_2}(j\omega) \quad (\text{A44})$$

where y_2 is the frequency domain representation of the incremental variation in $A_2(t)$.

By performing the divisions indicated in Eqs. A42 and A43 on Eqs. A34 and A35 and then carrying out the necessary substitution and rearrangement to eliminate unwanted state variables, it can be shown that the transfer functions for the x_1 - and x_2 -distortional components, defined by Eqs. A42 and A43, respectively, may be given in terms of the kinetic rate coefficients of the myofilament system as

$$H_{x_1}(j\omega) = \frac{1}{2} \frac{j\omega[j\omega + (h + g + h')]}{[j\omega]^2 + [h + f' + g + h']j\omega + f'[g + h']} \quad (\text{A45})$$

$$H_{x_2}(j\omega) = \frac{1}{2} \frac{j\omega[j\omega + (h + f' + g + h')]}{[j\omega]^2 + [h + f' + g + h']j\omega + f'[g + h']} \quad (\text{A46})$$

Further, substitution and rearrangement of Eqs. A33–A40 result in the following expression for the ε_2 recruitment component, defined by Eq. A44, in terms of kinetic features of the myofilament system,

$$H_{\varepsilon_2}(j\omega) = \frac{[n_5j\omega + n_4][H_{x_1}(j\omega)] + [n_3j\omega + n_2][H_{x_2}(j\omega)]}{[j\omega]^3 + k_2[j\omega]^2 + k_1j\omega + k_0} + \frac{n_1j\omega + n_0}{[j\omega]^3 + k_2[j\omega]^2 + k_1j\omega + k_0} \quad (\text{A47})$$

where the numerator coefficients, n_i , and denominator coefficients, k_i , are a combination of the $\partial_i^{Y_j}$ and $\partial_i^{U_m}$ (and these are, in turn, combinations of rate coefficients, reference states, and coefficients that grade the strength of the various nonlinearities). For the numerator coefficients.

$$n_0 = \partial_2^1 \partial_1^3 \partial_1^{u_2} - \partial_2^1 \partial_3^2 \partial_3^3$$

$$n_1 = \partial_2^1 \partial_1^{u_2}$$

$$n_2 = \partial_2^1 \partial_1^3 \partial_3^5 - \partial_2^1 \partial_1^5 \partial_3^3$$

$$n_3 = \partial_2^1 \partial_1^5$$

$$n_4 = \partial_2^1 \partial_1^3 \partial_3^4 - \partial_2^1 \partial_1^4 \partial_3^3$$

$$n_5 = \partial_2^1 \partial_1^4$$

For the denominator coefficients:

$$k_0 = -\partial_1^1 \partial_2^2 \partial_3^3 + \partial_2^2 \partial_1^3 \partial_3^1 + \partial_2^1 \partial_2^2 \partial_3^3 - \partial_2^1 \partial_1^3 \partial_3^2$$

$$k_1 = \partial_1^1 \partial_2^2 + \partial_2^2 \partial_3^3 + \partial_1^1 \partial_3^3 - \partial_1^1 \partial_3^1 - \partial_2^1 \partial_1^2$$

$$k_2 = -(\partial_1^1 + \partial_2^2 + \partial_3^3)$$

Using the 0 subscript to represent the value of the state variables at the steady-state reference condition, the $\partial_i^{Y_j}$ and $\partial_i^{U_m}$ are derived from Eqs. A1–A5 as

$$\partial_1^1 = -[h + f'] \quad (\text{A48})$$

$$\partial_1^2 = \frac{\partial f}{\partial A_2} D_0 - \frac{\partial f'}{\partial A_2} A_{10} + h' \quad (\text{A49})$$

$$\partial_1^3 = f \quad (\text{A50})$$

$$\partial_1^4 = \frac{\partial f}{\partial x_1} D_0 - \frac{\partial f'}{\partial x_1} A_{10} \quad (\text{A51})$$

$$\partial_1^5 = \frac{\partial f}{\partial x_2} D_0 - \frac{\partial f'}{\partial x_2} A_{10} \quad (\text{A52})$$

$$\partial_1^{u_2} = \frac{\partial f}{\partial L_S} D_0 - \frac{\partial f'}{\partial L_S} A_{10} \quad (\text{A53})$$

$$\partial_2^1 = h \quad (\text{A54})$$

$$\partial_2^2 = -(h' + g) \quad (\text{A55})$$

$$\partial_3^1 = \frac{\partial k_{\text{on}}}{\partial A_1} (R_{Z0} - A_{10} - A_{20} - D_0) - \frac{\partial k_{\text{off}}}{\partial A_1} D_0 + (f' - k_{\text{on}}) \quad (\text{A56})$$

$$\partial_3^2 = \frac{\partial k_{\text{on}}}{\partial A_2} (R_Z - A_{10} - A_{20} - D_0) + \frac{\partial f'}{\partial A_2} A_{10} - \left(\frac{\partial f}{\partial A_2} + \frac{\partial k_{\text{off}}}{\partial A_2} \right) D_0 + (g - k_{\text{on}}) \quad (\text{A57})$$

$$\partial_3^3 = \frac{\partial k_{\text{on}}}{\partial \mathbf{D}} (R_Z - A_{10} - A_{20} - D_0) - \frac{\partial k_{\text{off}}}{\partial \mathbf{D}} D_0 - (k_{\text{on}0} + k_{\text{off}0} + f_0) \quad (\text{A58})$$

$$\partial_3^4 = \frac{\partial k_{\text{on}}}{\partial x_1} (R_{Z0} - A_{10} - A_{20} - D_0) + \frac{\partial f'}{\partial x_1} A_{10} - \left(\frac{\partial f}{\partial x_1} + \frac{\partial k_{\text{off}}}{\partial x_1} \right) D_0 \quad (\text{A59})$$

$$\partial_3^5 = \frac{\partial k_{\text{on}}}{\partial x_2} (R_{Z0} - A_{10} - A_{20} - D_0) + \frac{\partial f'}{\partial x_2} A_{10} - \left(\frac{\partial f}{\partial x_2} + \frac{\partial k_{\text{off}}}{\partial x_2} \right) D_0 \quad (\text{A60})$$

$$\partial_3^{u_1} = \frac{\partial k_{\text{on}}}{\partial \text{Ca}} (R_{Z0} - D_0 - A_{10} - A_{20}) - \frac{\partial k_{\text{off}}}{\partial \text{Ca}} D_0 \quad (\text{A61})$$

$$\partial_3^{u_2} = \frac{\partial R_Z}{\partial L_S} k_{\text{on}} + \frac{\partial k_{\text{on}}}{\partial L_S} (R_Z - D_0 - A_{10} - A_{20}) - \frac{\partial k_{\text{off}}}{\partial L_S} D_0 + \frac{\partial f'}{\partial L_S} A_{10} - \frac{\partial f}{\partial L_S} D_0 \quad (\text{A62})$$

$$\partial_4^4 = -(h + f') \quad (\text{A63})$$

$$\partial_4^5 = h \quad (\text{A64})$$

$$\partial_4^{u_2} = \frac{j\omega}{2} \quad (\text{A65})$$

$$\partial_5^4 = g + h' \quad (\text{A66})$$

$$\partial_5^5 = -(g + h') \quad (\text{A67})$$

$$\partial_5^{u_2} = \frac{j\omega}{2} \quad (\text{A68})$$

and, the following partial derivatives are derived from Eqs. A18–A21,

$$\frac{\partial f}{\partial A_2} = f_{LS} \frac{1}{R_Z} (e^{(v-1)} - 1) 2 \left[1 + \frac{A_{20}}{R_Z} (e^{(v-1)} - 1) \right] \quad (\text{A69})$$

$$\frac{\partial f'}{\partial A_2} = f'_{LS} \frac{1}{R_Z} (e^{-(v-1)} - 1) 2 \left[1 + \frac{A_{20}}{R_Z} (e^{-(v-1)} - 1) \right] \quad (\text{A70})$$

$$\frac{\partial f}{\partial x_1} = f_{LS} \frac{A_{10}v - 1}{R_{Z0} x_0} 2 \left[1 + \frac{A_{20}}{R_{Z0}} (e^{(v-1)} - 1) \right] \quad (\text{A71})$$

$$\frac{\partial f'}{\partial x_1} = f'_{LS} \frac{A_{10}1 - v}{R_{Z0} x_0} 2 \left[1 + \frac{A_{20}}{R_{Z0}} \left(\frac{1}{e^{(v-1)}} - 1 \right) \right] \quad (\text{A72})$$

$$\frac{\partial f}{\partial x_2} = f_{LS} \frac{A_{20}v - 1}{R_{Z0} x_0} e^{(v-1)} 2 \left[1 + \frac{A_{20}}{R_{Z0}} (e^{(v-1)} - 1) \right] \quad (\text{A73})$$

$$\frac{\partial f'}{\partial x_2} = f'_{LS} \frac{A_{20}1 - v}{R_{Z0} x_0} \frac{1}{e^{(v-1)}} 2 \left[1 + \frac{A_{20}}{R_{Z0}} \left(\frac{1}{e^{(v-1)}} - 1 \right) \right] \quad (\text{A74})$$

$$\frac{\partial f}{\partial L_S} = f_0 \frac{\beta}{L_{S\text{ref}}} e^{\beta x_0} \quad (\text{A75})$$

$$\frac{\partial f'}{\partial L_S} = -f'_0 \frac{\beta}{L_{S\text{ref}}} e^{-\beta x_0} \quad (\text{A76})$$

$$\begin{aligned} \frac{\partial k_{\text{on}}}{\partial A_1} &= k_{\text{on}}^{\text{ref}} \frac{1}{R_Z} (u - 1) \\ &\times 2 \left[1 + \frac{D_0 + A_{10}}{R_Z} (u - 1) + \frac{A_{20}}{R_Z} (ue^{(w-1)} - 1) \right] \end{aligned} \quad (\text{A77})$$

$$\begin{aligned} \frac{\partial k_{\text{off}}}{\partial A_1} &= k_{\text{off}}^{\text{ref}} \frac{1}{R_Z} \left(\frac{1}{u} - 1 \right) \\ &\times 2 \left[1 + \frac{D_0 + A_{10}}{R_Z} \left(\frac{1}{u} - 1 \right) + \frac{A_{20}}{R_Z} \left(\frac{1}{ue^{(w-1)}} - 1 \right) \right] \end{aligned} \quad (\text{A78})$$

$$\begin{aligned} \frac{\partial k_{\text{on}}}{\partial A_2} &= k_{\text{on}}^{\text{ref}} \frac{1}{R_Z} (ue^{(w-1)} - 1) \\ &\times 2 \left[1 + \frac{D_0 + A_{10}}{R_Z} (u - 1) + \frac{A_{20}}{R_Z} (ue^{(w-1)} - 1) \right] \end{aligned} \quad (\text{A79})$$

$$\begin{aligned} \frac{\partial k_{\text{off}}}{\partial A_2} &= k_{\text{off}}^{\text{ref}} \frac{1}{R_Z} \left(\frac{1}{ue^{(w-1)}} - 1 \right) \\ &\times 2 \left[1 + \frac{D_0 + A_{10}}{R_Z} \left(\frac{1}{u} - 1 \right) + \frac{A_{20}}{R_Z} \left(\frac{1}{ue^{(w-1)}} - 1 \right) \right] \end{aligned} \quad (\text{A80})$$

$$\begin{aligned} \frac{\partial k_{\text{on}}}{\partial \mathbf{D}} &= k_{\text{on}}^{\text{ref}} \frac{1}{R_Z} (u - 1) \\ &\times 2 \left[1 + \frac{D_0 + A_{10}}{R_Z} (u - 1) + \frac{A_{20}}{R_Z} (ue^{(w-1)} - 1) \right] \end{aligned} \quad (\text{A81})$$

$$\begin{aligned} \frac{\partial k_{\text{off}}}{\partial \mathbf{D}} &= k_{\text{off}}^{\text{ref}} \frac{1}{R_Z} \left(\frac{1}{u} - 1 \right) \\ &\times 2 \left[1 + \frac{D_0 + A_{10}}{R_Z} \left(\frac{1}{u} - 1 \right) + \frac{A_{20}}{R_Z} \left(\frac{1}{ue^{(w-1)}} - 1 \right) \right] \end{aligned} \quad (\text{A82})$$

$$\begin{aligned} \frac{\partial k_{\text{on}}}{\partial x_1} &= k_{\text{on}}^{\text{ref}} \frac{w - 1}{x_0} \frac{A_{10}}{R_{Z0}} \\ &\times u 2 \left[1 + \frac{D_0 + A_{10}}{R_{Z0}} (u - 1) + \frac{A_{20}}{R_{Z0}} (ue^{(w-1)} - 1) \right] \end{aligned} \quad (\text{A83})$$

$$\frac{\partial k_{\text{off}}}{\partial x_1} = k_{\text{off}}^{\text{ref}} \frac{1-w}{x_0} \frac{A_{10}}{R_{Z0}} \frac{1}{u} \times 2 \left[1 + \frac{D_0 + A_{10}}{R_{Z0}} \left(\frac{1}{u} - 1 \right) + \frac{A_{20}}{R_{Z0}} \left(\frac{1}{ue^{(w-1)}} - 1 \right) \right] \quad (\text{A84})$$

$$\frac{\partial k_{\text{on}}}{\partial x_2} = k_{\text{on}}^{\text{ref}} u \frac{w-1}{x_0} e^{(w-1)} \frac{A_{20}}{R_{Z0}} \times 2 \left[1 + \frac{D_0 + A_{10}}{R_{Z0}} (u-1) + \frac{A_{20}}{R_{Z0}} (ue^{(w-1)} - 1) \right] \quad (\text{A85})$$

$$\frac{\partial k_{\text{off}}}{\partial x_2} = k_{\text{off}}^{\text{ref}} \frac{1}{ue^{(w-1)}} \frac{(1-w)}{x_0} \frac{A_{20}}{R_{Z0}} \times 2 \left[1 + \frac{D_0 + A_{10}}{R_{Z0}} \left(\frac{1}{u} - 1 \right) + \frac{A_{20}}{R_{Z0}} \left(\frac{1}{ue^{(w-1)}} - 1 \right) \right] \quad (\text{A86})$$

$$\frac{\partial k_{\text{on}}}{\partial \text{Ca}} = (k_{\text{on}}^{\text{Ca}} - k_{\text{on}}^0) \left[\frac{\text{Ca}_{50}}{(\text{Ca}_{50} + \text{Ca}_0)^2} \right] \times \left[1 + \frac{D_0 + A_{10}}{R_Z} (u-1) + \frac{A_{20}}{R_Z} (ue^{(w-1)} - 1) \right]^2 \quad (\text{A87})$$

$$\frac{\partial k_{\text{off}}}{\partial \text{Ca}} = (k_{\text{off}}^{\text{Ca}} - k_{\text{off}}^0) \left[\frac{\text{Ca}_{50}}{(\text{Ca}_{50} + \text{Ca}_0)^2} \right] \times \left[1 + \frac{D_0 + A_{10}}{R_Z} \left(\frac{1}{u} - 1 \right) + \frac{A_{20}}{R_Z} \left(\frac{1}{ue^{(w-1)}} - 1 \right) \right]^2 \quad (\text{A88})$$

$$\frac{\partial R_Z}{\partial L_S} = \begin{cases} \frac{R_T}{L_M - B} & \text{if } L_S < (2L_A - B) \\ 0 & \text{if } (2L_A - B) < L_S < (2L_A + B) \\ -\frac{R_T}{L_M - B} & \text{if } L_S > (2L_A + B) \end{cases} \quad (\text{A89})$$

$$\frac{\partial k_{\text{on}}}{\partial L_S} = k_{\text{on}}^{\text{ref}} \left(-\frac{\partial R_Z}{\partial L_S} \right) \frac{1}{R_{Z0}^2} \times 2[(D_0 + A_{10})(u-1) + A_{20}(ue^{(w-1)} - 1)] \quad (\text{A90})$$

$$\frac{\partial k_{\text{off}}}{\partial L_S} = k_{\text{off}}^{\text{ref}} \left(-\frac{\partial R_Z}{\partial L_S} \right) \frac{1}{R_{Z0}^2} \times 2 \left[(D_0 + A_{10}) \left(\frac{1}{u} - 1 \right) + A_{20} \left(\frac{1}{ue^{(w-1)}} - 1 \right) \right] \quad (\text{A91})$$

REFERENCES

- Abbot, R. H., and G. J. Steiger. 1977. Temperature and amplitude dependence of tension transient in glycerinated skeletal and insect fibrillar muscle. *J. Physiol.* 266:13–42.
- Berman, M. R., J. N. Peterson, D. T. Yue, and W. C. Hunter. 1988. Effect of isoproterenol on force transient time course and on stiffness spectra in rabbit papillary muscle in barium contracture. *J. Mol. Cell Cardiol.* 20:415–426.
- Blanchard, E., C. Seidman, J. G. Seidman, M. LeWinter, and D. Maughan. 1999. Altered crossbridge kinetics in the $\alpha\text{MHC}^{403/+}$ mouse model of familial hypertrophic cardiomyopathy. *Circ. Res.* 84:475–483.
- Campbell, K. 1997. Rate constant of muscle force redevelopment reflects cooperative activation as well as cross-bridge kinetics. *Biophys. J.* 72:254–262.
- Campbell, K. B., H. Taheri, R. D. Kirkpatrick, T. Burton, and W. C. Hunter. 1993. Similarities between dynamic elastance of left ventricular chamber and papillary muscle of rabbit heart. *Am. J. Physiol. Heart Circ. Physiol.* 264:H1926–H1941.
- Campbell, K. B., M. V. Razumova, R. D. Kirkpatrick, and B. K. Slinker. 2001. Myofilament kinetics in isometric twitch dynamics. *Ann. Biomed. Eng.* 29:384–405.
- Dickinson, M. H., C. J. Hyatt, F.-O. Lehmann, J. R. Moore, M. C. Reedy, A. Simcox, R. Tohtong, J. O. Vigoreaux, H. Yamashita, and D. W. Maughan. 1997. Phosphorylation-dependent power output of transgenic flies: an integrated study. *Biophys. J.* 73:3122–3134.
- Fuchs, F., and S. H. Smith. 2001. Calcium, cross-bridges, and the Frank-Starling Relationship. *News Physiol. Sci.* 16:5–10.
- Godt, R. E., and D. W. Maughan. 1981. Influence of osmotic compression on calcium activation and tension in skinned muscle fibers of he rabbit. *Pflugers Arch.* 391:334–337.
- Huxley, A. F., and R. M. Simmons. 1971. Proposed mechanism of force generation in striated muscle. *Nature.* 233:533–538.
- Huxley, A. F. 1957. Muscle structure and theories of contraction. *Prog. Biophys. Biophys. Chem.* 7:255–318.
- Kawai, M., and H. R. Halvorson. 1989. Role of MgATP and MgADP in the cross-bridge kinetics in chemically skinned rabbit psoas fibers. Study of a fast exponential process. *Biophys. J.* 55:595–603.
- Kawai, M., and P. Brandt. 1980. Sinusoidal analysis: a high resolution method for correlating biochemical reactions with physiological processes in activated skeletal muscles of rabbit, frog and crayfish. *J. Mus. Res. & Cell Motil.* 1:279–304.
- Kawai, M., Y. Saeki, and Y. Zhao. 1993. Crossbridge scheme and the kinetic constants of elementary steps deduced from chemically skinned papillary and trabecular muscles of the ferret. *Circ. Res.* 73:35–50.
- McDonald, K. S., and R. L. Moss. 1995. Osmotic compression of single cardiac myocytes eliminates the reduction in Ca^{2+} sensitivity of tension at short sarcomere length. *Circ. Res.* 77:199–205.
- Machin, K. E., and J. W. S. Pringle. 1960. The physiology of insect fibrillar muscle. III. The effect of sinusoidal of changes of length on a beetle flight muscle. *Proc. R. Soc. Lond. B.* 152:311–330.
- Maughan, D., J. Moore, J. Vigoreaux, B. Barnes, and L. A. Mulieri. 1998. Work production and work absorption in muscle strips from vertebrate cardiac and insect flight muscle fibers. In *Mechanisms of Work Production and Work Absorption in Muscle*. H. Sugi and G. Pollack, editors. Plenum Press, New York. 471–480.
- Murase, M., H. Tanaka, K. Nishiyama, and H. Shimizu. 1986. A three-state model for oscillation in muscle: sinusoidal analysis. *J. Musc. Res. Cell. Motil.* 7:2–10.
- Pringle, J. W. S. 1978. Stretch activation of muscle: function and mechanism. *Proc. R. Soc. Lond.* 201:107–130.
- Razumova, M. V., A. E. Bukatina, and K. B. Campbell. 1999. Stiffness-distortion sarcomere model for muscle simulation. *J. Appl. Physiol.* 87:1861–1876.
- Razumova, M. V., A. E. Bukatina, and K. B. Campbell. 2000. Different myofilament nearest-neighbor interactions have distinctive effects on contractile behavior. *Biophys. J.* 78:3120–3137.

- Rossmannith, G. H., J. F. Y. Hoh, A. Kirman, and L. J. Kwan. 1986. Influence of V1 and V3 isomyosins on the mechanical behavior of rat papillary muscle as studied by pseudo-random binary noise modulated length perturbations. *J. Musc. Res. Cell Motil.* 7:307–319.
- Saeiki, Y., M. Kawai, and Y. Zhao. 1991. Comparison of crossbridge dynamics between intact and skinned myocardium from ferret right ventricles. *Circ. Res.* 68:772–781.
- Shibata, T., W. C. Hunter, and K. Sagawa. 1987. Dynamic stiffness of barium-contracted cardiac muscles with different speeds of contraction. *Circ. Res.* 60:770–779.
- Smith, D. A. 1990. The theory of sliding filament models for muscle contraction. III. Dynamics of the five-state model. *J. Theor. Biol.* 146: 433–466.
- Steiger, G. J. 1971. Stretch activation and myogenic oscillation of isolated contractile structures of heart muscle. *Pflugers Arch.* 330:347–361.
- Thomas, N., and R. A. Thornhill. 1996. Stretch activation and nonlinear elasticity of muscle cross-bridge. *Biophys. J.* 70:2807–2818.
- Thorson, J., and D. C. White. 1983. Role of cross-bridge distortion in the small-signal mechanical dynamics of insect and rabbit striated muscle. *J. Physiol.* 343:59–84.
- Wannenburg, T., G. H. Heijne, J. H. Geerdink, H. W. Van den Dool, P. M. L. Janssen, and P. P. deTombe. 2000. Cross-bridge kinetics in rat myocardium: effect of sarcomere length and calcium activation. *Am. J. Physiol. Heart. Circ. Physiol.* 279:H779–H790.
- Zhao, Y., and M. Kawai. 1993. The effect of lattice spacing change on cross-bridge kinetics in chemically skinned rabbit psoas muscle. Elementary steps affected by the spacing change. *Biophys. J.* 64:197–210.
- Zhao, Y., and M. Kawai. 1996. Inotropic agent EMD-53998 weakens nucleotide and phosphate binding to cross bridges in porcine myocardium. *Am. J. Physiol. Heart Circ. Physiol.* 271:H1394–H1406.